Investigation of Natural convection and Entropy Generation of non-Newtonian flow in Molten Polymer-filled Odd-Shaped Cavities using FDLBM

Saba Y. Ahmed[1], Qusay Rasheed Al-Amir[1], Hameed K. Hamzah[1], Farooq H. Ali[1], Azher M. Abed[2], Ahmed Al-Manea[3], Karim Egab[4], Raed Al-Rbaihat[5], Khalid Saleh[6, *], Ali Alahmer[5,7, *]

[1]Mechanical Engineering Department, College of Engineering, Babylon University, Babylon, Iraq.

[2]Air Conditioning and Refrigeration Techniques Engineering Department Al-Mustaqbal University College, Babylon 51001, Iraq.

[3]Department of Mechanical Engineering, Al-Furat Al-Awsat Technical University, Iraq.

[4]Southern Technical University, Thiqar Technical College, Iraq.

[5]Department of Mechanical Engineering, Faculty of Engineering, Tafila Technical University, Tafila 66110, Jordan.

[6]School of Engineering, University of Southern Queensland, Toowoomba, QLD 4350, Australia.

[7]Department of Industrial and Systems Engineering, Auburn University, Auburn, AL 36849, United State.

* Correspondence: Khalid.Saleh@usq.edu.au (Khalid Saleh); aza0300@auburn.edu (Ali Alahmer)

Abstract

This study examines the natural convection heat transfer (NCHT) and entropy generation (EG) of a non-Newtonian (NN) flow inside an odd-shaped cavity filled with molten polymer. The cavity configuration comprises hot internal walls, cold external walls, and insulated remaining walls. The Finite Difference Lattice Boltzmann Method (FDLBM) is employed to solve the involving governing equations. The input parameters span a range of values, with Rayleigh number (Ra) varying from 10^4 to 10^5, power-law index (n) covering a range from 0.5 to 1.5, and width ratio (WR) ranging from 0.2 to 0.4, while maintaining Prandtl number (Pr) at a constant value of 10. The results revealed that at Ra values of 10^4 and 10^5, the overall entropy increases as the WR increases from 0.2 to 0.4 and decreases as the n index increases. In contrast to dilatant fluids, where heat transfer (HT) decreases as the n index increases from 1 to 1.5, pseudo-plastic fluids show an opposite trend with HT increasing as the n index decreases from 1 to 0.5. This trend is attributed to the general decrease in the average Nusselt number (Nu) as the n index increases. Additionally, it is observed that the n index has no significant impact on the average Nu due to low buoyancy force at Ra = 10^4 and WRs of 0.2 and 0.3. However, it notably influences the Be across all width ratios. Overall, the present model demonstrates excellent agreement with previous numerical results, affirming the FDLBM as a superior, reliable, and well-suited technique for relevant applications. These results suggest the potential to extend the application of the

FDLBM approach to various cavity shapes, allowing for a comprehensive exploration of NCHT and EG under various conditions.

Keywords: Natural Convection, Odd-Shaped Cavity, FDLBM, Non-Newtonian, Molten Polymer, Dimensionless numbers

1. Introduction

Recent technological advancements have directed the attention of designers toward optimizing fluid dynamics and cavity design. In particular, the utilization of molten polymers has gained prominence for boosting heat transfer (HT) and fluid behavior within cavities during the fabrication of thermoplastics and thermosets for engineering applications [1–3]. The behavior of molten polymers can be simulated using the non-Newtonian (NN) power-law model [4]. As a result, a significant number of scientists are currently keen on exploring convective HT in materials governed by NN power-law behaviors. A fundamental and critical challenge in the field of fluid mechanics revolves around buoyancy-driven flow within cavities. This challenge has found widespread utilization in various technical applications and scholarly investigations, with the NN power-law model being extensively applied [5,6]. Consequently, the study of natural convection heat transfer (NCHT) within fluids characterized by NN power laws has been a focal point of numerous numerical studies. Kim et al. [7] examined the transient NCHT of fluids with NN power laws in a square container with differently heated walls. The results showed that the average Nusselt number (Nu) rises with a diminishing power-law index (n) for a Prandtl number (Pr) ranging from 10^2 to 10^4 and a Rayleigh number (Ra) ranging from 10^5 to 10^7. Ohta et al. [8] studied the pseudo-plastic fluids' NCHT rate in a square cavity with cold top and heated bottom walls. The authors pointed out that pseudo-plastic fluids' NCHT rate rises when stable vortex flows occur compared to Newtonian fluids. A two-dimensional study of NCHT in an inclined rectangular slot with short side walls exposed to homogeneous heat flow was conducted by Lamsaadi et al. [9]. The outcomes demonstrated the significant impact of cavity orientation on the HT rate for a given Ra. Specifically, when the cavity was heated from the bottom, it exhibited the highest heat transfer capacity, while heating from the top resulted in only a modest convective flow. Furthermore, they noted that changes in the inclination angle had a pronounced influence on convection HT, especially as n decreased. Lamsaadi et al. [10] studied the stability of NCHT in a horizontal rectangular container filled with NN power-law fluids using both numerical and analytical methods. The computational results were supported by analytical research, revealing that shear-thinning enhances HT and fluid flow, while shear-thickening has the opposite effect. Turan et al. [11] investigated the two-dimensional steady-state laminar convective HT within square cavities filled with NN fluids. The cavities featured differentially heated sidewalls and constant wall temperatures. The results showed that the average Nu increased as the Ra rose for both Newtonian and power-law

fluids. Conversely, an increase in n corresponded to a decrease in the average Nu. Furthermore, the simulation results demonstrated that an increase in the Pr had a negligible impact on the average Nu across a range of Ra and n index values, regardless of whether the fluids exhibited Newtonian or power-law behavior. Two-dimensional steady-state NCHT of a fluid with a NN power-law was investigated by Matin et al. [12]. The study focused on the HT between two uniformly square, horizontal, equilateral ducts, with temperature being held constant. The results showed a weak correlation between eccentricity and Nu, highlighting that this correlation was influenced by various other factors. Furthermore, with a few exceptions, adjusting the Pr has no impact on heat transmission properties. Khezzar et al. [13] conducted a numerical analysis of NCHT within a two-dimensional slanted rectangular enclosure, considering both Newtonian and NN power-law type fluids. The findings demonstrated that shear thickening and shear thinning led to a significant decrease and increase, respectively, in the heat transfer (HT) rate when compared to a Newtonian fluid. Additionally, it was observed that for shear-thickened or shear-thinned fluids, variations in parameters such as aspect ratio (AR), n index, Pr, and Ra had an impact on the average Nu. Matin and Khan [14] conducted a numerical investigation into steady-state NCHT in power-law fluids within two concentrically arranged horizontal cylinders with varying temperatures. The results indicated that, particularly in cooling and insulating applications, pseudo-plastic and dilatant fluids outperformed Newtonian fluids. Moreover, as the Ra increased, the insulating effect of dilatant fluids and the cooling effect of pseudo-plastic fluids became more pronounced.

The Lattice Boltzmann Method (LBM) has proven to be a powerful technique, applied extensively to investigate a wide array of phenomena, encompassing turbulent flow, magnetohydrodynamic flow, porous media, nanofluids, ferrofluids, and more [15–23]. Nevertheless, its applicability for NN fluids, particularly regarding the energy equations, is constrained [24]. The Finite Difference Lattice Boltzmann Method (FDLBM), a derivative of LBM, emerges as a more appropriate solution. FDLBM can effectively formulate shear stress equations in a classical manner. It demonstrates the capability to successfully solve various energy equations involving NN fluids. In contrast to conventional LBM, FDLBM operates independently of the relaxation period while preserving the advantages associated with the LBM approach. Kefayati [25] investigated the effects of a magnetic field (Mag. Fld.) on NN blood flow using FDLBM. The investigation specifically assessed the influence of varying Stuart and Reynolds numbers on the flow using a power-law model for the NN fluid. In another study, Kefayati [26] used FDLBM to analyze the impact of a Mag. Fld. on the flow of NN blood between two annuli of square concentric ducts. The findings demonstrated that the influence of the Mag. Fld. became more pronounced as the n index decreased. Furthermore, the vertical Mag. Fld. exerted a more significant influence on the primary circulation within the cavity compared to the horizontal Mag. Fld.

Additionally, as the size of the inner cylinder varied from A = L/4 to L/2, the impact of the Mag. Fld. on fluid flow within the cavity diminished. Kefayati [27] utilized the FDLBM to explore the NCHT of molten NN polymer within a square cavity featuring a sinusoidally heated wall. A power-law model was employed to represent the behavior of the NN fluid, considering n indices (n = 0.5 to 1.5) and Ra values (Ra = 104 and 105). The results demonstrate that FDLBM proved to be an effective approach for addressing this complex problem. Furthermore, the heat transfer reduced as the n index increased. Furthermore, it was observed that Ra = 10^5 exerted a slightly more substantial influence on heat transmission compared to Ra = 10^4. Jabbar et al. [28] numerically investigated the effects of wavy interface wall and layer thickness on the thermal and flow fields for the differentially heated square enclosure with two sections (an NN material and an Ag/water nanofluid porous medium). The study encompassed various parameters, including Ra (Ra = 10^3 to 10^5), the number of undulations (N = 1 to 4), Pr of water (Pr = 6.2), volume fraction ($0 \leq \varphi \leq 0.2$), Darcy number (Da = 10^{-1} to 10^{-5}), n index (n = 0.6 to 1.4), and various interface locations (F = 0.25, 0.5, and 0.75). The investigation involved the development of equations describing streamlines and isotherms through the solution of governing equations using the Galerkin finite element method (GFEM). The study outcomes exhibited strong alignment with previous research, demonstrating that the average Nu decreases as the n index increases, primarily due to the high shear force and viscosity associated with pseudo-plastic fluids. The HT rate was significantly affected by changes in layer thickness but exhibited only a relatively minor sensitivity to alterations in the number of undulations. Aboud et al. [29] employed the GFEM to investigate fluid flow and convective heat transfer within a circular annulus filled with NN Cu-water nanofluid. The study encompassed a range of parameters, including the Hartman number ($0 \leq Ha \leq 60$), Richardson number ($0 \leq Ri \leq 1$), φ ($0 \leq \varphi \leq 1$), and the n index ($0.2 \leq n \leq 1.4$). The Grashof number (Gr = 100) and Pr (Pr = 6.2) were held as constants. The inner stationary cylinder maintained a hot temperature, while the outer rotating cylinder was kept at a cold temperature. The ratio of the inner circular diameter to the annulus space length was held at a constant value of 2. The findings revealed that when the stream function increased with a rising n index (n = 1), the fluid behavior resembled that of a Newtonian fluid. Additionally, the presence of a Mag. Fld. exerted a substantial influence on fluid flow patterns, and as forced convection improved, the average Nu increased in response to decreasing Ri. Al-Mensoury et al. [30] numerically investigated the NCHT of an NN nanofluid in an F-shaped porous cavity. The right wall of the enclosure was consistently kept at a low temperature, while the left wall was consistently heated. The remaining walls of the cavity were assumed to be insulated. The study was conducted using COMSOL Multiphysics and employed the GFEM. The findings demonstrated a significant impact of nanoparticles on HT rates. As the AR increased, the interior regions of the cavities reduced in size, resulting in the formation of stagnation zones and a shorter

distance between the hot and cold walls. Ali et al. [31] studied the effects of various factors, including a Mag. Fld., AR of cold baffles, inclination angle, Ra, Ha, n index, and nanoparticle volume fraction, on the flow and HT of an NN nanofluid in a baffled U-shaped cavity. The study employed different computational methods based on the GFEM. The bottom wall of the cavity was heated using a sine-wave profile, while the remaining walls were thermally insulated. The results revealed that the n index significantly influenced the Nu for Ra = 10^6, with its impact diminishing at lower values of Ra. It was also observed that when the Ha was below 30, both the n index and Ha had a significant impact on HT. An increase in the n index resulted in a 5% increase for AR = 0.4 and a 7% increase for AR = 0.6 below a certain nanoparticle threshold. In a study conducted by Jassim et al. [32], the impact of aluminum oxide (Al_2O_3) nanoparticles on HT rates in four different enclosures was explored using the finite element method. The study considered a range of parameters, including Ha ($0 \leq Ha \leq 60$), Ri ($0.001 \leq Ri \leq 1$), n indices ($0.2 \leq n \leq 1.4$), φ ($0 \leq φ \leq 0.1$), while maintaining a constant Gr (Gr = 100). The study introduced an innovative boundary condition involving a unique heating geometry of the wall, resulting in an alternating effect when altering the n index and Ri. However, it was noted that the strength of the Mag. Fld. negatively impacted forced convection within the enclosure. The study also found that the average Nu increased due to the rising n index, regardless of the shape geometry of the heating cavity wall. Hussein et al. [33] conducted a numerical analysis to investigate the NCHT within an F-shaped cavity filled with NN nanofluid consisting of Ag-water and saturated by a porous medium. In the study, the right wall of the cavity maintained a constant low temperature, while the left wall was consistently heated and exposed to a periodic horizontal Mag. Fld. The top and bottom walls were thermally insulated. The study explored various parameters, including Ra ($10^3 \leq Ra \leq 10^6$), periodic shape parameter ($0.1 \leq λ \leq 1$), AR ($0.1 \leq AR \leq 0.4$), Da ($10^{-5} \leq Da \leq 10^{-1}$), φ ($0 \leq φ \leq 0.06$), and n index ($0.6 \leq n \leq 1.4$). The results indicated that an increase in parameters such as φ, Da, and Ra led to an increase in the average Nu. Conversely, an increase in the n index and Ha resulted in a decrease in the average Nu. The relationship between Nu and the λ was found to be dependent on the values of the n index and Ra.

Based on the information available in the existing literature, no prior works have used the FDLBM technique to examine the interactions between NCHT and entropy generation (EG) in an odd-shaped cavity filled with NN liquid polymer and heated by a sinusoidal wall. This study attempts to address this knowledge gap and offers novel insights highlighting the unique challenges and phenomena associated with such configurations. Maximizing the NCHT within enclosures and minimizing the amount of EG is essential in various applications. This could be accomplished by filling the enclosures with molten polymer. This phenomenon is recognized to be crucial in enhancing the overall thermal systems performance. The findings of this study provide valuable insights into the NCHT phenomena

within enclosures, offering insightful information on the interaction between NCHT and EG under varying conditions. The current study aims to investigate numerically the NCHT and EG of an NN flow inside an odd-shaped cavity filled with molten polymer. The significance of this study is emphasized by highlighting the benefit of further understanding unique difficulties and physical phenomena corporates with NCHT within enclosures. Therefore, a better understanding of this area can enhance the overall thermal systems performance for a wide range of modern industrial applications, including solar collectors, nuclear reactor systems, steam power plants, heat exchangers, thermal energy storage systems, electronic cooling systems, and others. In the present configuration, the internal walls maintain a high temperature, the external walls remain cold, and all other walls are insulated. The FDLBM is employed to solve the involving governing equations. The model outcomes are cross-validated with earlier numerical findings, and the primary parameters under investigation include Ra, Nu, WR, n, Pr, Bejan number (Be), and total entropy (S_T) due to heat transfer ($S_{T, HT}$).

2. Mathematical Formulation

2.1. Definition of a Physical Problem

Figure 1 depicts a schematic illustration of the NCHT occurring within an irregularly shaped cavity filled with a NN molten polymer. The cold and hot surfaces have a length of "L", which can be oriented either vertically or horizontally. The width of the enclosure, represented as "W", is variable and defined by the width ratio "WR", where "WR" equals "W/L". The exterior walls, depicted in blue, are subject to cooling through a sinusoidal temperature function "T_c", while the internal walls maintain a constant hot surface temperature "T_h". The remaining two sides are thermally insulated.
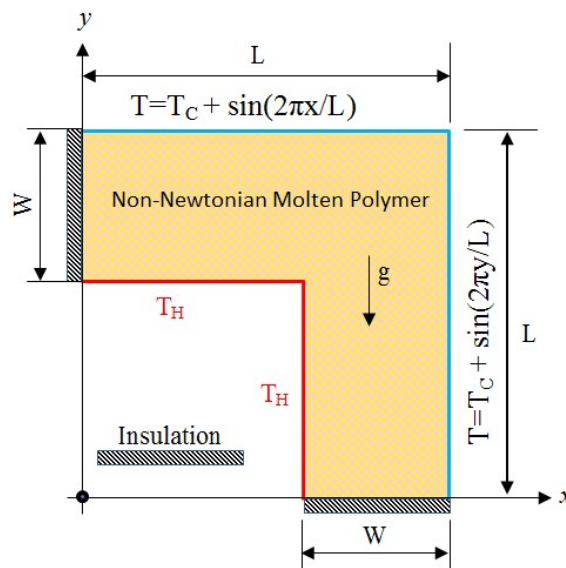
Figure 1. Schematic geometry of the present study.

2.2. Governing Equation and Boundary Conditions

This study focuses on a two-dimensional NCHT fluid flow occurring within an irregular-shaped cavity filled with a NN molten polymer. The fluid flow is assumed to be steady, incompressible, and laminar, with a constant Pr of 10. The effects of viscous dissipation and radiation have been neglected, while the gravitational force is considered to act vertically downwards. Accordingly, the governing equations in dimensional form for the Boussinesq approximation model can be expressed as Equations (1 to 4) [27].

$$\frac{\partial \ddot{u}}{\partial \ddot{x}} + \frac{\partial \ddot{v}}{\partial \ddot{y}} = 0 \tag{1}$$

$$\frac{\partial \ddot{u}}{\partial t} + \ddot{u}\frac{\partial \ddot{u}}{\partial \ddot{x}} + \ddot{v}\frac{\partial \ddot{u}}{\partial \ddot{y}} = -\frac{1}{\rho}\frac{\partial \ddot{p}}{\partial \ddot{x}} + \frac{1}{\rho}\left[\frac{\partial}{\partial \ddot{x}}(\tau_{\ddot{x}\ddot{x}}) + \frac{\partial}{\partial \ddot{y}}(\tau_{\ddot{x}\ddot{y}})\right] \tag{2}$$

$$\frac{\partial \ddot{v}}{\partial t} + \ddot{u}\frac{\partial \ddot{v}}{\partial \ddot{x}} + \ddot{v}\frac{\partial \ddot{v}}{\partial \ddot{y}} = -\frac{1}{\rho}\frac{\partial \ddot{p}}{\partial \ddot{y}} + \frac{1}{\rho}\left[\frac{\partial}{\partial \ddot{x}}(\tau_{\ddot{x}\ddot{y}}) + \frac{\partial}{\partial \ddot{y}}(\tau_{\ddot{y}\ddot{y}})\right] + g\beta(T - T_c) \tag{3}$$

$$\frac{\partial T}{\partial t} + \ddot{u}\frac{\partial T}{\partial \ddot{x}} + \ddot{v}\frac{\partial T}{\partial \ddot{y}} = \alpha\left(\frac{\partial^2 T}{\partial \ddot{x}^2} + \frac{\partial^2 T}{\partial \ddot{y}^2}\right) \tag{4}$$

The analysis of the purely viscous NN fluid is conducted using the Ostwald-de Waele model, which describes the shear stress tensor as expressed in Equations 5 and 6 [34].

$$\tau_{ij} = \ddot{\mu}_a\left(\frac{\partial \ddot{u}_i}{\partial \ddot{x}_j} + \frac{\partial \ddot{u}_j}{\partial \ddot{x}_i}\right) \tag{5}$$

Where $\ddot{\mu}_a$ is the apparent viscosity and it calculated as follows [35].

$$\ddot{\mu}_a = K\left\{2\left[\left(\frac{\partial \ddot{u}}{\partial \ddot{x}}\right)^2 + \left(\frac{\partial \ddot{v}}{\partial \ddot{y}}\right)^2\right] + \left(\frac{\partial \ddot{v}}{\partial \ddot{x}} + \frac{\partial \ddot{u}}{\partial \ddot{y}}\right)^2\right\}^{\frac{n-1}{2}} \tag{6}$$

The boundary conditions for the present configuration are described in Equation 7.

At the internal walls: $T = T_h$

At the external walls: $T = \begin{cases} T_c + (T_h - T_c).\sin(2\pi\ddot{x}/L) & \text{n for right vertical wall} \\ T_c + (T_h - T_c).\sin(2\pi\ddot{y}/L) & \text{for top horizontal wall} \end{cases}$ \tag{7}

At the rest of the surfaces: $\frac{\partial T}{\partial N} = 0$

At all solid walls: $\ddot{u} = \ddot{v} = 0$

To numerically solve the governing equations with boundary conditions, the non-dimensional variables are defined in Equation 8.

$$\bar{X} = \frac{\ddot{x}}{L}, \bar{Y} = \frac{\ddot{y}}{L}, \bar{U} = \frac{\ddot{u}}{\left(\frac{\alpha}{L}\right).Ra^{0.5}}, \bar{V} = \frac{\ddot{v}}{\left(\frac{\alpha}{L}\right).Ra^{0.5}}, \bar{P} = \frac{\ddot{p}}{\rho\left(\frac{\alpha}{L}\right)^2 Ra}, \bar{t} = \frac{t}{\left(\frac{L^2}{\alpha}\right).Ra^{-0.5}}, \bar{\theta} = \frac{T-T_c}{T_h-T_c}, \; Ra =$$

$$\frac{\rho.\beta.g_y.L^3(T_h-T_c)}{v.\alpha} \;, Pr = \frac{\ddot{\mu}_a}{\rho.\alpha} \tag{8}$$

When using non-dimensional variables, the non-dimensional governing equations are expressed in Equations 9 to 12.

$$\frac{\partial\bar{U}}{\partial\bar{X}} + \frac{\partial\bar{V}}{\partial\bar{Y}} = 0 \tag{9}$$

$$\frac{\partial\bar{U}}{\partial\bar{t}} + \bar{U}\frac{\partial\bar{U}}{\partial\bar{X}} + \bar{V}\frac{\partial\bar{U}}{\partial\bar{Y}} = -\frac{\partial P}{\partial\bar{X}} + \frac{Pr}{\sqrt{Ra}}\left[2\frac{\partial}{\partial\bar{X}}\left(\frac{\mu_a}{K}\frac{\partial\bar{U}}{\partial\bar{X}}\right) + \frac{\partial}{\partial\bar{Y}}\left(\frac{\mu_a}{K}\left(\frac{\partial\bar{U}}{\partial\bar{X}} + \frac{\partial\bar{V}}{\partial\bar{Y}}\right)\right)\right] \tag{10}$$

$$\frac{\partial\bar{V}}{\partial\bar{t}} + \bar{U}\frac{\partial\bar{V}}{\partial\bar{X}} + \bar{V}\frac{\partial\bar{V}}{\partial\bar{Y}} = -\frac{\partial P}{\partial\bar{Y}} + \frac{Pr}{\sqrt{Ra}}\left[2\frac{\partial}{\partial\bar{Y}}\left(\frac{\mu_a}{K}\frac{\partial\bar{V}}{\partial\bar{Y}}\right) + \frac{\partial}{\partial\bar{X}}\left(\frac{\mu_a}{K}\left(\frac{\partial\bar{U}}{\partial\bar{Y}} + \frac{\partial\bar{V}}{\partial\bar{X}}\right)\right)\right] + Pr\bar{\theta} \tag{11}$$

$$\frac{\partial\bar{\theta}}{\partial\bar{t}} + \bar{U}\frac{\partial\bar{\theta}}{\partial\bar{X}} + \bar{V}\frac{\partial\bar{\theta}}{\partial\bar{Y}} = \frac{1}{\sqrt{Ra}}\left(\frac{\partial^2\bar{\theta}}{\partial\bar{X}^2} + \frac{\partial^2\bar{\theta}}{\partial\bar{Y}^2}\right) \tag{12}$$

The apparent viscosity as a function of shear rate, denoted as μ_a, is defined in Equation13.

$$\mu_a = K\left\{2\left[\left(\frac{\partial\bar{U}}{\partial\bar{X}}\right)^2 + \left(\frac{\partial\bar{V}}{\partial\bar{Y}}\right)^2\right] + \left(\frac{\partial\bar{V}}{\partial\bar{X}} + \frac{\partial\bar{U}}{\partial\bar{Y}}\right)^2\right\}^{\frac{n-1}{2}} \tag{13}$$

Where K is the consistency coefficient.

$$n = \begin{cases} = 1 & Newtonian\ fluids \\ < 1 & Pseudo-plastic\ fluids\ (Shear\ Thining) \\ > 1 & Dilatant\ fluids\ (Shear\ Thickening) \end{cases}$$

The apparent viscosity of dilatant fluids increases with increasing shear rate, whereas the apparent viscosity of pseudo-plastic fluids decreases with increasing shear rate. The non-dimensional boundary conditions are stated in Equation 14.

At the internal walls: $\bar{\theta} = 1$

At the external walls: $\bar{\theta} = \begin{cases} \sin(2\pi\bar{X}) & \text{for right vertical wall} \\ \sin(2\pi\bar{Y}) & \text{for top horizontal wall} \end{cases}$ \hfill (14)

At the rest of the surfaces: $\frac{\partial\bar{\theta}}{\partial N} = 0$

At all solid walls: $\ddot{U} = \ddot{V} = 0$

The average Nu (Nu_{ave}) along the heated internal surfaces is employed to define the overall HT rate across the cavity, as stated in Equation 15.

$$Nu_{ave} = \frac{1}{1 - W_R} \int_{\bar{Y}=0}^{\bar{Y}=1-W_R} \left[\frac{\partial \bar{\theta}}{\partial \bar{X}}\right]_{X=1-W_R} dY + \int_{\bar{X}=0}^{\bar{X}=1-W_R} \left[\frac{\partial \bar{\theta}}{\partial \bar{Y}}\right]_{Y=1-W_R} dX \qquad (15)$$

The local EG rate in dimensionless form is summation of EG due to two sources, heat flow and fluid friction, as described in Equations (16 to 18) [36,37].

$$\dot{S}_{gen,HT} = \frac{K}{T_0^2}\left[\left(\frac{\partial \bar{\theta}}{\partial \bar{X}}\right)^2 + \left(\frac{\partial \bar{\theta}}{\partial \bar{Y}}\right)^2\right] \qquad (16)$$

$$\dot{S}_{gen,FF} = \frac{\mu_{no}}{KT_0}\left[(\bar{U}^2 + \bar{V}^2) + \Gamma\left\{2\left[\left(\frac{\partial \bar{U}}{\partial \bar{X}}\right)^2 + \left(\frac{\partial \bar{V}}{\partial \bar{Y}}\right)^2\right] + \left(\frac{\partial \bar{U}}{\partial \bar{Y}} + \frac{\partial \bar{V}}{\partial \bar{X}}\right)^2\right\}\right] \qquad (17)$$

$$\dot{S}_{gen} = \dot{S}_{gen,HT} + \dot{S}_{gen,FF} \qquad (18)$$

Where $T_O = \frac{T_h + T_c}{2}$, and the value of Γ in Equation 17 is the irreversibility factor. Integrating the local EG across all computing domains yields the dimensionless total EG, as specified in Equation 19.

$$S_{gen} = \dot{S}_{gen}.\frac{L_c^2}{k_f}\left(\frac{T_0}{(T_h - T_c)}\right)^2 \qquad (19)$$

The Be is a measure of the degree of irreversibility brought on by the EG during heat transport based on Equation 20 [38].

$$Be_T = \frac{\dot{S}_{gen,HT}}{S_{gen}} \qquad (20)$$

Where the Be has three cases, which are:

$$Be = \begin{cases} = \frac{1}{2} & S_{gen,FF} = S_{gen,HT} \\ \ll \frac{1}{2} & S_{gen,FF} \\ = 1 & S_{gen,HT} \end{cases}$$

3. Numerical Procedure

3.1. Lattice Boltzmann Method (LBM)

In this study, the governing equations of two-dimensional NCHT fluid flow in an oddly shaped cavity filled with NN molten polymer are solved using the LBM with specified boundary conditions. The method employed by Kefayati [39] utilizes the finite difference approach and the splitting method to separate the

Boltzmann equation, allowing for the calculation of shear stresses in the flow fields. Unlike conventional LBM, this approach enables the application of various boundary conditions without restrictions. The outcome of the LBM is represented by a normalized discrete Boltzmann equation, as illustrated in Equation 21.

$$\frac{\partial f_k}{\partial t} + c_k . \nabla f_k = \Omega_k \qquad k = 0; \ldots; 8 \tag{21}$$

where f_k, c_k and Ω_k are the discrete particle distribution function, the discrete particle velocity, and the rate of change of distribution function f_k, respectively. The right-hand term, Ω_k can be approximated based on Equation 22.

$$\Omega_k = -\frac{1}{\epsilon\omega}(f_k - f_k^{eq}) \tag{22}$$

where ϵ, ω and f_k^{eq}, respectively, represent for time step, relaxation time, and discrete particle equilibrium distribution function. In the standard procedure, the LBM comprises of two primary steps: streaming and collisions. If Eq. (22) has been split using the splitting method, and the relaxation time has been set to one ($\omega = 1$), the streaming step can be calculated according to Equation 23.

$$\frac{\partial f_k}{\partial t} + c_k . \nabla_{\ddot{x}} f_k = 0 \tag{23}$$

Equation 24 was solved using the Lax–Wendroff method, which represents the collisions step without the need for a forcing function [40].

$$\frac{\partial f_k}{\partial t} = -\frac{1}{\epsilon\omega}(f_k(\ddot{x}, t) - f_k^{eq}(\ddot{x}, t)) \tag{24}$$

The outcome of the streaming step serves as the initial conditions for solving the collision step. By selecting $\epsilon = \Delta t$ and $\omega = 1$, the Euler technique can be used to simplify Equation 24, as demonstrated in Equation 25.

$$f_k^{eq}(\ddot{x}, t) = f_k(\ddot{x}, t + \Delta t) \tag{25}$$

The expansion of f_k is characterized as of the Chapman-Enskog type, as defined in Equation 26.

$$f_k = f_k^{eq} + \epsilon\, f_k^1 + \epsilon^2\, f_k^2 + o(\epsilon^3) \tag{26}$$

The macroscopic fluid density and velocities, denoted as c_k and weighted by the distribution function, are expressed in Equations 27 to 30.

$$\rho = \sum_{k=0}^{8} f_k^{eq} \ , \quad \ddot{u} = \frac{1}{\rho}\sum_{k=0}^{8} f_k^{eq} \ c_{kx} \text{ and } \quad \ddot{v} = \frac{1}{\rho}\sum_{k=0}^{8} f_k^{eq} \ c_{ky} \tag{27}$$

Also,

$$\rho\ddot{u}^2 + \ddot{p} - \tau_{\ddot{x}\ddot{x}} = \sum_{k=0}^{8} f_k^{eq} \ c_{kx}^2 \tag{28}$$

$$\rho\ddot{v}^2 + \ddot{p} - \tau_{\ddot{y}\ddot{y}} = \sum_{k=0}^{8} f_k^{eq} \ c_{ky}^2 \tag{29}$$

$$\rho\ddot{u}\ddot{v} - \tau_{\ddot{x}\ddot{y}} = \sum_{k=0}^{8} f_k^{eq} \ c_{kx}c_{ky} \tag{30}$$

For incompressible fluids, the normalized NS equations are expressed in Equations 31 to 33.

$$\frac{\partial}{\partial t}(\rho) + \frac{\partial}{\partial \ddot{x}}(\rho\ddot{u}) + \frac{\partial}{\partial \ddot{y}}(\rho\ddot{v}) = 0 \tag{31}$$

$$\frac{\partial}{\partial t}(\rho\ddot{u}) + \frac{\partial}{\partial \ddot{x}}(\rho\ddot{u}^2) + \frac{\partial}{\partial \ddot{y}}(\rho\ddot{u}\ddot{v}) = -\frac{\partial}{\partial \ddot{x}}(\ddot{p}) + \frac{\partial}{\partial \ddot{x}}(\tau_{\ddot{x}\ddot{x}}) + \frac{\partial}{\partial \ddot{x}}(\tau_{\ddot{x}\ddot{y}}) + o(\epsilon) \tag{32}$$

$$\frac{\partial}{\partial t}(\rho\ddot{v}) + \frac{\partial}{\partial \ddot{y}}(\rho\ddot{v}^2) + \frac{\partial}{\partial \ddot{x}}(\rho\ddot{u}\ddot{v}) = -\frac{\partial}{\partial \ddot{y}}(\ddot{p}) + \frac{\partial}{\partial \ddot{y}}(\tau_{\ddot{y}\ddot{y}}) + \frac{\partial}{\partial \ddot{x}}(\tau_{\ddot{x}\ddot{y}}) + o(\epsilon) \tag{33}$$

Where ρ denotes the fluid density, which is taken to remain constant. The letters u and v are represented the $\ddot{x}$ and $\ddot{y}$ velocity components, respectively. $\ddot{p}$ is pressure, and $\tau_{\ddot{x}\ddot{x}}$, $\tau_{\ddot{y}\ddot{y}}$, $\tau_{\ddot{x}\ddot{y}}$ are the shear stress components of the flow.

To solve the Navier-Stokes equations based on Equation 25 with an error term of O ($\in$), a suitable $\boldsymbol{f_k^{eq}}$ based on Equations (27 to 30) should be defined. The conventional technique is not used in this initial attempt to create a workable $\boldsymbol{f_k^{eq}}$ for microscale flows. It is anticipated that c_k will have a polynomial series up to the second, as expressed in Equation 34.

$$f_k^{eq} = A_k + (c_k)_{\ddot{x}}A\ddot{x}_k + (c_k)_{\ddot{y}}A\ddot{y}_k + (c_k)_{\ddot{x}}^2 \ B\ddot{x}\ddot{x}_k + (c_k)_{\ddot{y}}^2 \ B\ddot{y}\ddot{y}_k + (c_k)_{\ddot{x}}.(c_k)_{\ddot{y}}B\ddot{x}\ddot{y}_k \tag{34}$$

The Maxwell distribution function is typically enlarged to include terms up to the second or third order with respect to the product of $\ddot{u}$ and c_k. The equilibrium distribution function ($\boldsymbol{f_k^{eq}}$)) in this study differs from conventional ones used by earlier scholars. The particle velocity, c_k, can be stated in Equation 35 [41].

$$c_k\Gamma = \begin{cases} 0 & k = 0 \\ \left\{\cos(i-1)\frac{\pi}{2}, \ \sin(i-1)\frac{\pi}{2}\right\}, k = 1,3,5,7 \\ \Gamma\sqrt{2}\left\{\cos(i-5)\frac{\pi}{2}+\frac{\pi}{4}, \ \sin(i-5)\frac{\pi}{2}+\frac{\pi}{4}\right\}, k = 2,4,6,8 \end{cases} \tag{35}$$

The numerical stability must be considered when choosing the constant (Γ). A detailed procedure for determining this parameter is provided in [42]. The parameters for the equilibrium distribution function (f_k^{eq}) are defined as shown in Equations 36a to 36f.

$$A_0 = \rho - \frac{2p}{\Gamma^2} - \frac{p|u|^2}{\Gamma^2} + \frac{\tau_{\ddot{x}\ddot{x}}+\tau_{\ddot{y}\ddot{y}}}{\Gamma^2}, A_1 = A_2 = 0 \tag{36a}$$

$$A\ddot{x}_1 = \frac{\rho\ddot{u}}{2\Gamma^2}, A\ddot{x}_2 = 0 \tag{36b}$$

$$A\ddot{y}_1 = \frac{\rho\ddot{v}}{2\Gamma^2}, A\ddot{y}_2 = 0 \tag{36c}$$

$$B\ddot{x}\ddot{x}_1 = \frac{1}{2\Gamma^4}\left(\ddot{p} + \rho\ddot{u}^2 - \tau_{\ddot{x}\ddot{x}}\right), \ B\ddot{x}\ddot{x}_2 = 0 \tag{36d}$$

$$Byy_1 = \frac{1}{2\Gamma^4}\left(\ddot{p} + \rho\ddot{v}^2 - \tau_{\ddot{y}\ddot{y}}\right), \ B\ddot{y}\ddot{y}_2 = 0 \tag{36e}$$

$$Bxy_2 = \frac{1}{4\Gamma^4}\left(\rho\ddot{u}\ddot{v} - \tau_{\ddot{x}\ddot{y}}\right), \ B\ddot{x}\ddot{y}_1 = 0, i,j = \ddot{x}, \ddot{y} \tag{36f}$$

The coefficients in Equation 34, A_k, $A\ddot{x}_k$, $A\ddot{y}_k$, $B\ddot{x}\ddot{x}_k$, $B\ddot{y}\ddot{y}_k$ and $B\ddot{x}\ddot{y}_k$ can be simplified as follows, assuming that parameters with the same magnitude of c_k are equal, as described in Equations 37 and 38.

$$\begin{aligned} A_1 &= A_3 = A_5 = A_7; \ A_2 = A_4 = A_6 = A_8 \\ A\ddot{x}_1 &= A\ddot{x}_3 = A\ddot{x}_5 = A\ddot{x}_7 \ ; \ A\ddot{x}_2 = A\ddot{x}_4 = A\ddot{x}_6 = A\ddot{x}_8 \\ A\ddot{y}_1 &= A\ddot{y}_3 = A\ddot{y}_5 = A\ddot{y}_7 \ ; \ A\ddot{y}_2 = A\ddot{y}_4 = A\ddot{y}_6 = A\ddot{y}_8 \\ A\ddot{x}\ddot{x}_1 &= A\ddot{x}\ddot{x}_3 = A\ddot{x}\ddot{x}_5 = A\ddot{x}\ddot{x}_7 \ ; \ A\ddot{x}\ddot{x}_2 = A\ddot{x}\ddot{x}_4 = A\ddot{x}\ddot{x}_6 = A\ddot{x}\ddot{x}_8 \\ A\ddot{y}\ddot{y}_1 &= A\ddot{y}\ddot{y}_3 = A\ddot{y}\ddot{y}_5 = A\ddot{y}\ddot{y}_7 \ ; \ A\ddot{y}\ddot{y}_2 = A\ddot{y}\ddot{y}_4 = A\ddot{y}\ddot{y}_6 = A\ddot{y}\ddot{y}_8 \\ A\ddot{x}\ddot{y}_1 &= A\ddot{x}\ddot{y}_3 = A\ddot{x}\ddot{y}_5 = A\ddot{x}\ddot{y}_7 \ ; \ A\ddot{x}\ddot{y}_2 = A\ddot{x}\ddot{y}_4 = A\ddot{x}\ddot{y}_6 = A\ddot{x}\ddot{y}_8 \end{aligned} \tag{37}$$

$$\tau_{ij} = \frac{Pr.\mu_a}{K\sqrt{Ra}}\left(\frac{\partial\ddot{u}_i}{\partial j} + \frac{\partial\ddot{u}_j}{\partial i}\right), i,j = \ddot{x}, \ddot{y} \text{ and } \ddot{u}_i = \ddot{u}, \ddot{u}_j = \ddot{v} \tag{38}$$

Equations 39 and 40 should be introduced into the streaming step to calculate the buoyancy force based on the momentum equation.

$$F_k = A_k + (c_k)_x A\ddot{x}_k + (c_k)_y A\ddot{y}_k \tag{39}$$

$$A_0 = A_1 = A_2 = 0$$

$$A\ddot{x}_1 = 0, \ A\ddot{x}_2 = 0 \tag{40}$$

$$A\ddot{y}_1 = \frac{Pr.T}{2\Gamma^2}, A\ddot{y}_2 = 0$$

The temperature field can be represented by the following polynomial, similar to the flow field, in accordance with the equilibrium distribution function, as described in Equations 41 and 42.

$$q_k^{eq} = A_k + (c_k)_{\dot{x}} A\ddot{x}_k + (c_k)_{\dot{y}} A\ddot{y}_k \tag{41}$$

$$A_0 = T, and \ A_1 = A_2 = 0$$

$$A\ddot{x}_1 = \frac{(\ddot{u}T - \frac{1}{\sqrt{Ra}}\frac{\partial T}{\partial \ddot{x}})}{2\Gamma^2}, \ A\ddot{x}_2 = 0 \ and \ A\ddot{y}_1 = \frac{(\ddot{v}T - \frac{1}{\sqrt{Ra}}\frac{\partial T}{\partial \ddot{y}})}{2\Gamma^2}, A\ddot{y}_2 = 0 \tag{42}$$

3.2. Grid Size Sensitivity and Model Validation

The grid sensitivity analysis was conducted for the average Nu and the absolute maximum streamlines, as presented in Table 1. The parameters used were n = 0.5, WR = 0.4, and Ra = 10^4. The grid size was incrementally increased from 3200 to 45000 evenly spaced nodes in both directions. A uniform grid size of 33800 (referred to as G8) was chosen for generating the numerical results. The refined mesh structure is depicted in Figure 2. To validate the current results, a comparative analysis was conducted against the outcomes obtained by Kefayati [27]. This validation involved the examination of streamlines and isotherm contours for a two-dimensional NCHT scenario in an NN molten polymer-filled square cavity, as depicted in Figure 3. The results indicated a significant convergence between the two studies. Additionally, Table 2 provides a comparison of the average Nu between this study and the results of Kefayati [27] for different n values and Ra = 10^4.

Table 1. Grid independent test showing the average Nu on the hot surface at (n = 0.5, WR = 0.4, and Ra = 10^4).

Grid	Domain elements	Boundary elements	Time (sec)	Nu $_{ave}$	$|Error|\%$
G1	3200	240	17	3.4142	-
G2	5000	300	20	3.4121	0.061
G3	7200	360	26	3.4099	0.0645
G4	9800	420	36	3.4072	0.079
G5	12800	480	46	3.4033	0.114
G6	20000	600	55	3.4002	0.091
G7	28800	720	117	3.3965	0.108

G8	33800	780	150	3.3955	0.030
G9	45000	900	196	3.3953	0.005
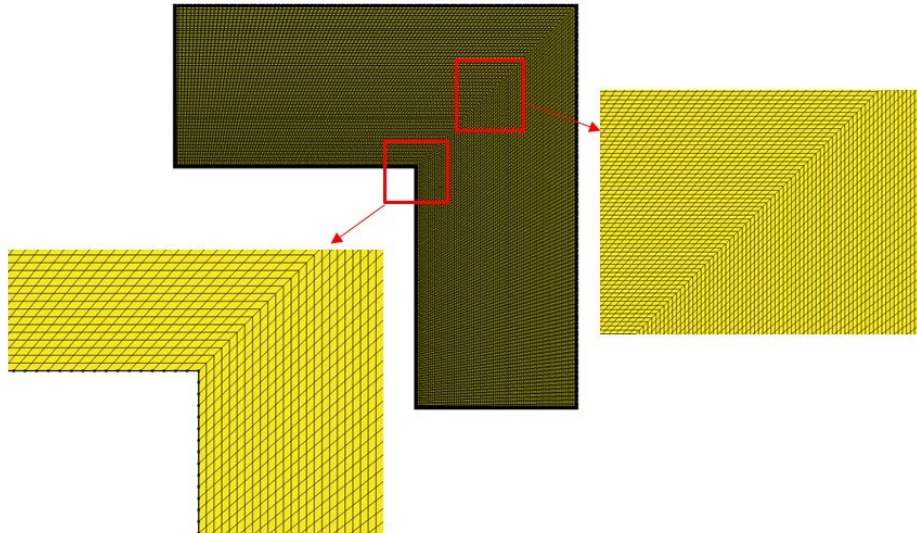
Figure 2. Mapped mesh structure.

Table 2. Comparative analysis of the average Nu between the current study and previous numerical results by Kefayati [27], for a different n at Ra = 10^4.

n	Average Nu at the hot wall		Error (%)
	Present study	Kefayati [27]	
0.5	2.9102	2.91	- 0.006
0.7	2.5368	2.53	-0.268
1	2.2374	2.23	- 0.33
1.3	2.0746	2.07	- 0.22
1.5	2.0031	2	-0.155
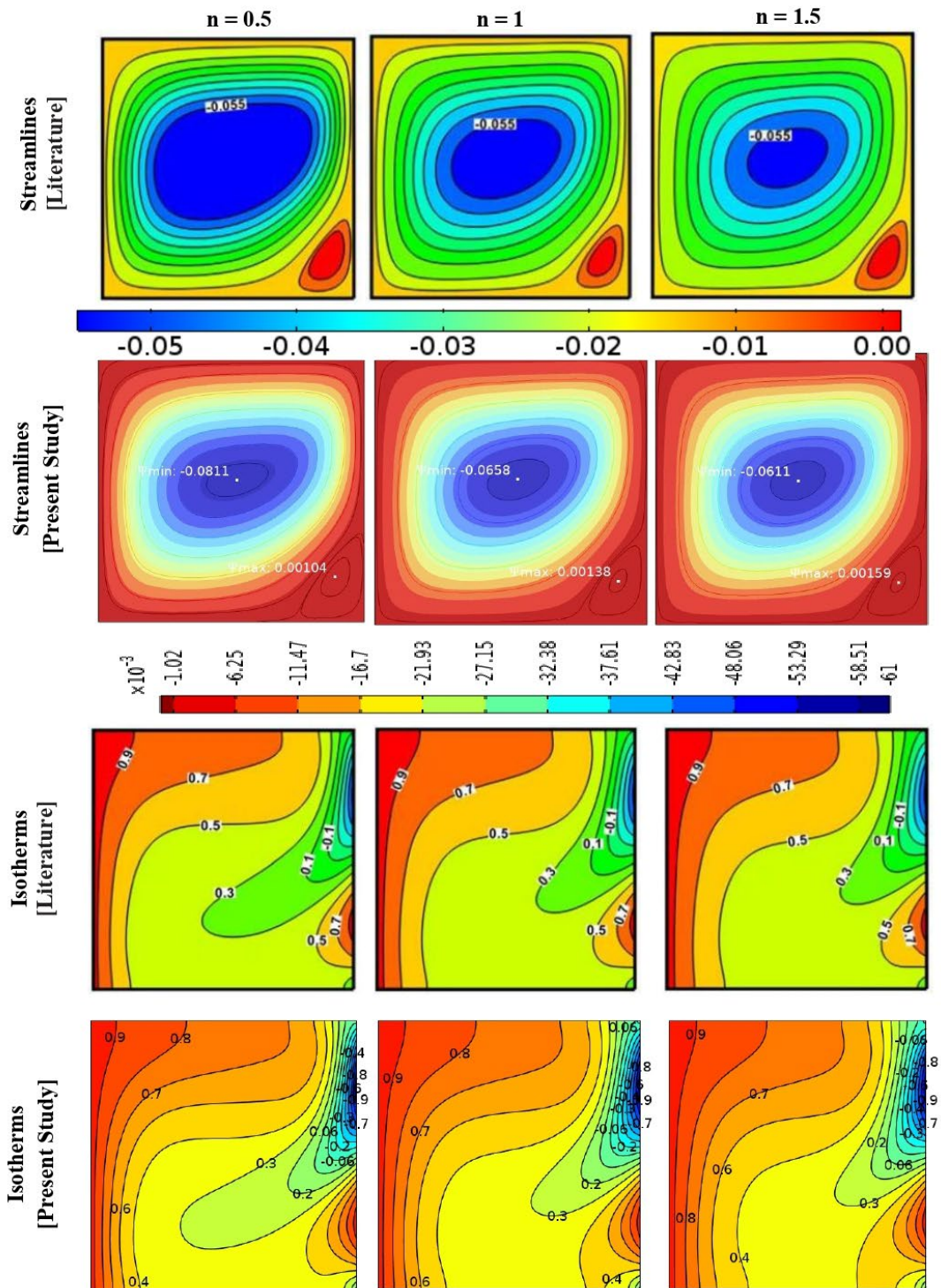
Figure 3. Comparative analysis of streamlines and isotherms features between the characteristics between the current study and previous computational results by Kefayati [27].

4. Results and Discussions

In this study, the FDLBM was employed to simulate the NCHT EG within an L-shaped cavity filled with an NN molten polymer. The simulations covered a range of Ra values (Ra = 104 and 105) and n indices (n = 0.5, 1, and 1.5), providing a comprehensive examination of the FDLBM approach.

Figure 4 illustrates the streamlines within the irregular cavity filled with NN fluid at Ra = 10^4, depicting various n indices and WRs. Notably, the minimum streamlines (Ψ_{min}) show an increase (from -0.0037 to -0.05245) with the rise in WR, transitioning from four rotating vortices at WR = 0.2 to two cells at WR = 0.4. Additionally, a decrease in the n index results in larger streamlines within the cavity. The number of streamlines in the core of the cavity serves as a reliable indicator of the enhanced convective flow associated with a lower n index. At WR = 0.4, where Ψ_{min} reaches -0.05245, the streamlines widen significantly due to the substantial reduction in the n index. Furthermore, for various Ra values, it is evident that the highest stream function in the case of a pseudo-plastic fluid (n = 0.5) is notably greater than that of a Newtonian fluid, highlighting the impact of the pseudo-plastic nature of the fluid on the streamlines. Similarly, for various WRs, the highest stream function for a pseudo-plastic fluid surpasses that of a Newtonian fluid. However, it is noteworthy that in the case of the middle streamline (n = 1.5), the shear-thickening fluid's flow travels less than the Newtonian fluid within the cavity, mainly due to the buoyancy force associated with dilatant flow.

The impact of the n index on the expansion of streamlines at Ra = 10^5 is depicted in Figure 5. It is observed that as the n index decreases, the expansion of streamlines for WR = 0.4 increases, reaching a value of 0.05478. The influence of Ra = 10^5 on stream functions is more pronounced than that of Ra = 10^4 for all WRs, as the non-dimensional velocity in the y-direction rises with increasing Ra. This leads to a heightened buoyancy effect, resulting in smoother fluid circulation in the cavity. Conversely, the magnitude of velocity decreases when the n index rises due to increased shear stress between adjacent fluid layers caused by shear thickening. For fluids with (n < 1), especially when the n index decreases, the buoyant force surpasses viscous flow resistance, primarily due to shear thinning. In contrast, as the n index increases for shear-thickening fluids (n > 1), convection effects become less significant than viscous forces.

n = 0.5   **n = 1**   **n = 1.5**

WR = 0.2

$\Psi_{max} = 4.227E-4$
$\Psi_{min} = -0.0037$

$\Psi_{max} = 7.420E-5$
$\Psi_{min} = -0.0052$

$\Psi_{max} = 7.969-4$
$\Psi_{min} = -0.0033$

WR = 0.3

$\Psi_{max} = 1.721E-4$
$\Psi_{min} = -0.02064$

$\Psi_{max} = 7.180E-5$
$\Psi_{min} = -0.01194$

$\Psi_{max} = 0.00125$
$\Psi_{min} = -0.00989$

WR = 0.4

$\Psi_{max} = 1.834E-4$
$\Psi_{min} = -0.05245$

$\Psi_{max} = 6.346E-4$
$\Psi_{min} = -0.02982$

$\Psi_{max} = 0.001053$
$\Psi_{min} = -0.02317$
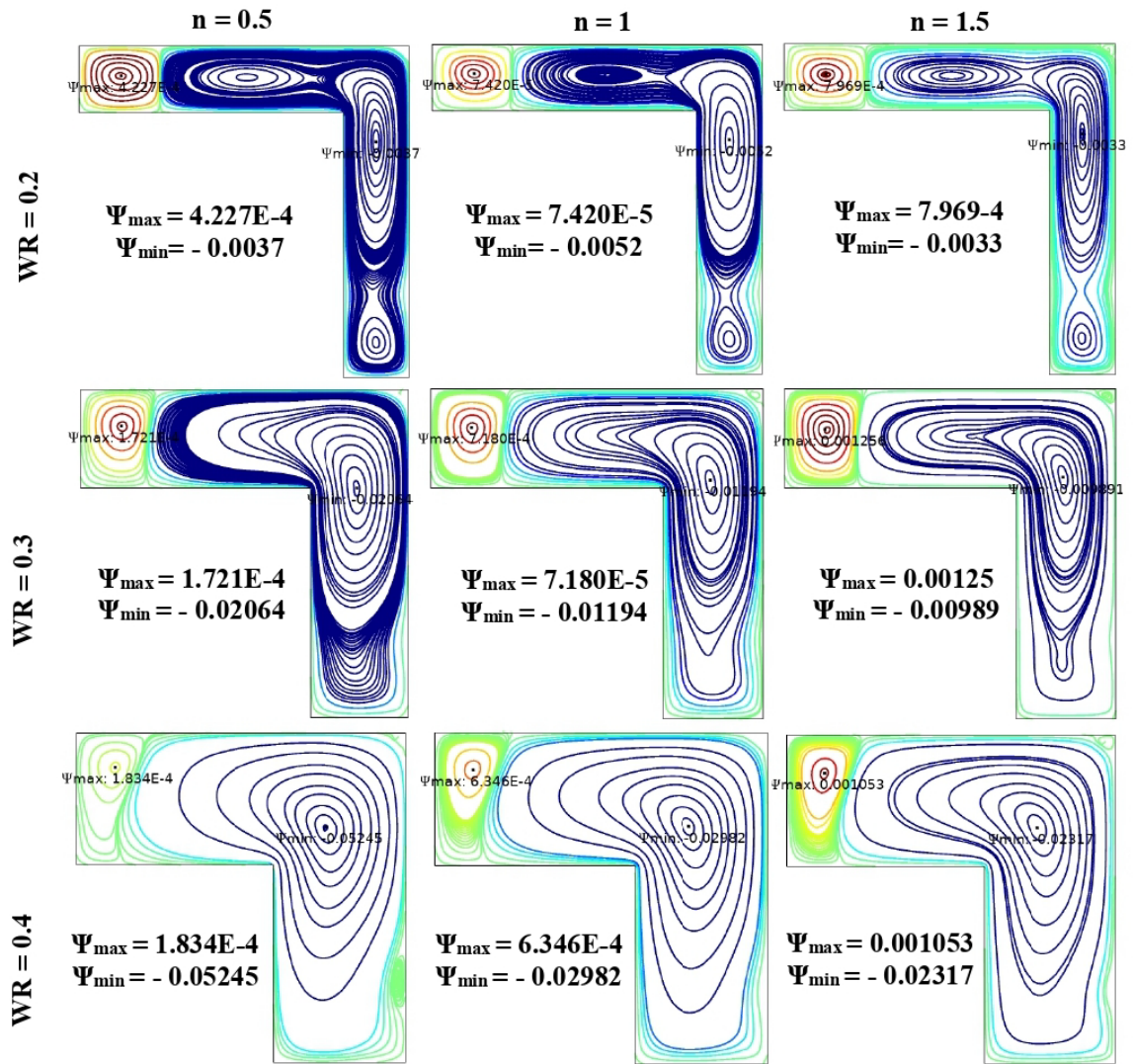
Figure 4. Streamlines contours different index number (n) and width ratio (WR) at Ra = 10^4.
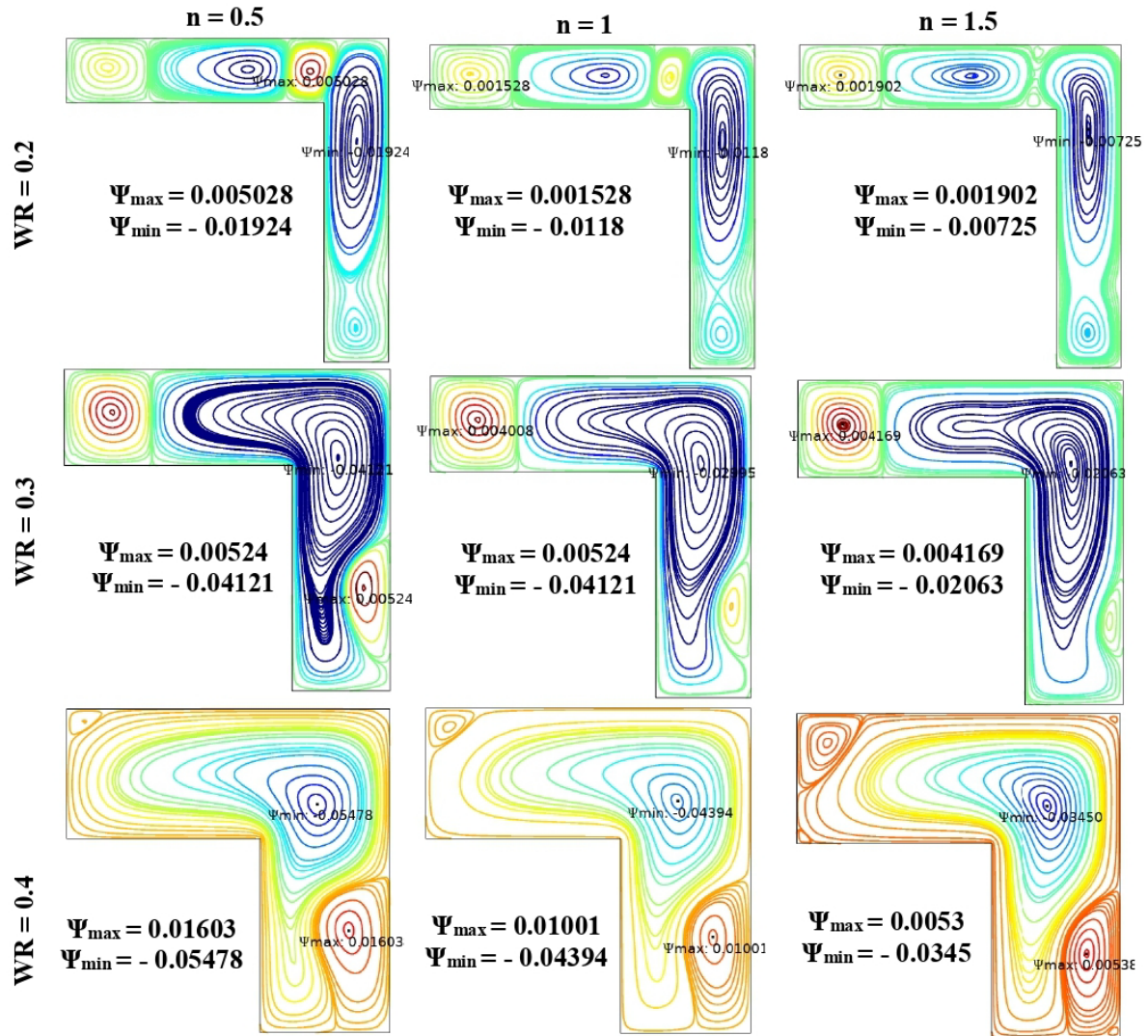
Figure 5. Streamlines contours different index number (n) and width ratio (WR) at Ra = 10^5.

The effect of WR on isothermal lines at Ra = 10^4 and 10^5 is presented in Figures 6 and 7, respectively. It is observed that with increasing WR, the temperature contours in the central region of the cavity extend further outward, especially at low n indices. For both Ra values, the rate of energy transfer steadily decreases as the n indices increase. This implies that the convective process slows down as the n index rises, causing the fluid within the cavity to move more slowly, particularly evident at Ra = 10^5, as depicted in Figure 7.
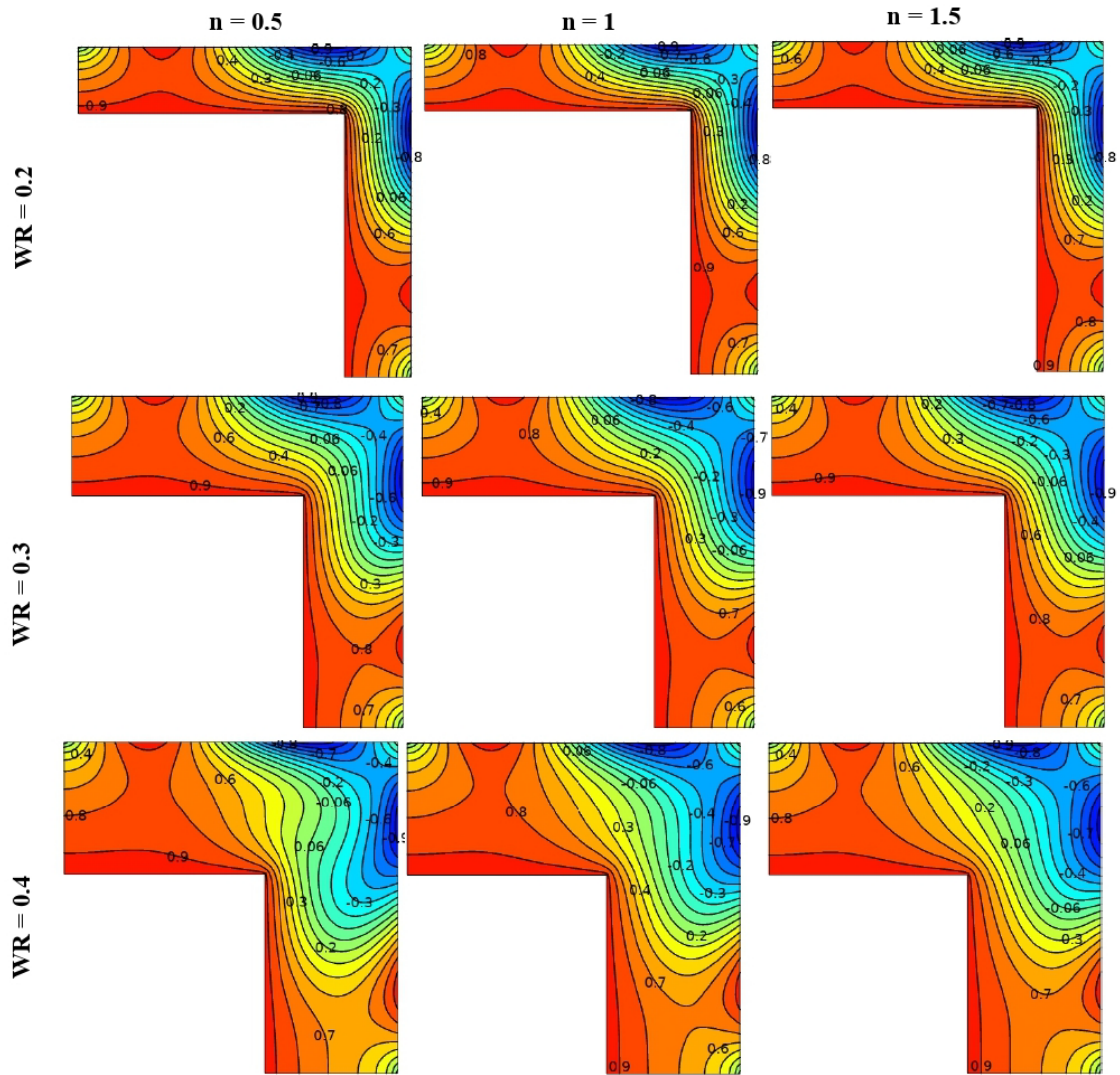
Figure 6. Isotherms contours for different index number (n) and width ratio (WR) at Ra = 10^4.
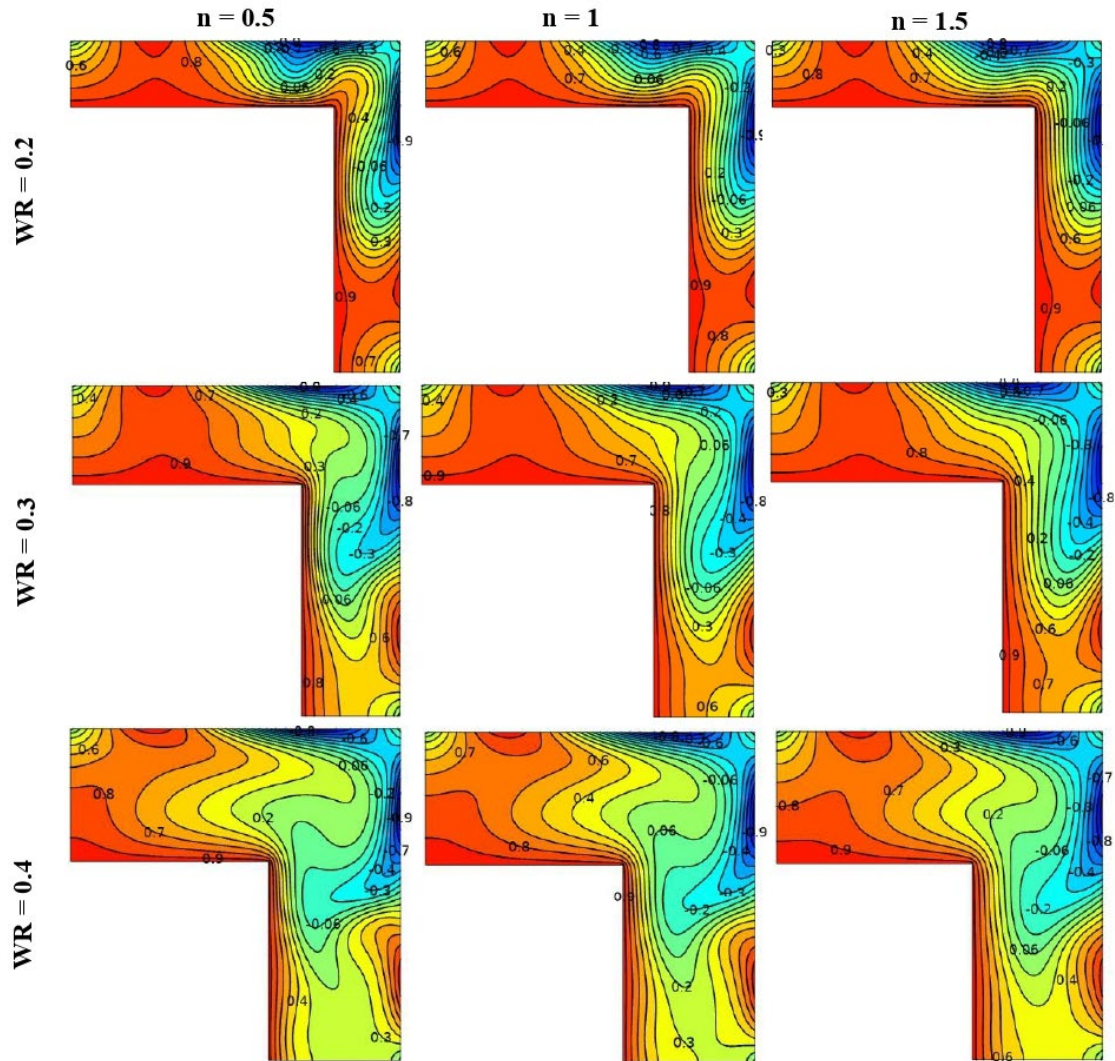
Figure 7. Isotherms contours for different index number (n) and width ratio (WR) at Ra = 10^5.

Figure 8 displays the Bejan number (Be) and total entropy due to heat transfer ($S_{T, HT}$) for different Ra values (Ra = 10^4 and 10^5) and power-law index values (n = 0.5, 1, and 1.5) at WR = 0.2. The Bejan number was previously defined as the ratio of HT irreversibility to the combined irreversibility of HT and fluid friction. As the Ra increases for a shear-thinning fluid with an n index of 0.5, the irreversibility of HT decreases, resulting in a higher Be. This suggests that the increase in HT irreversibility is more significant than the total irreversibility, especially noticeable at an n index of 0.5. However, as the n index increases and approaches a Newtonian or thickening fluid level, the total irreversibility decreases, causing the Be to increase for all WRs. Additionally, with increasing WR, the total irreversibility (HT and fluid friction) increases more than the irreversibility of HT alone, leading to a decrease in the Be. Similar trends at WR = 0.3 and 0.4 can be observed in Figures 9 and 10, respectively.
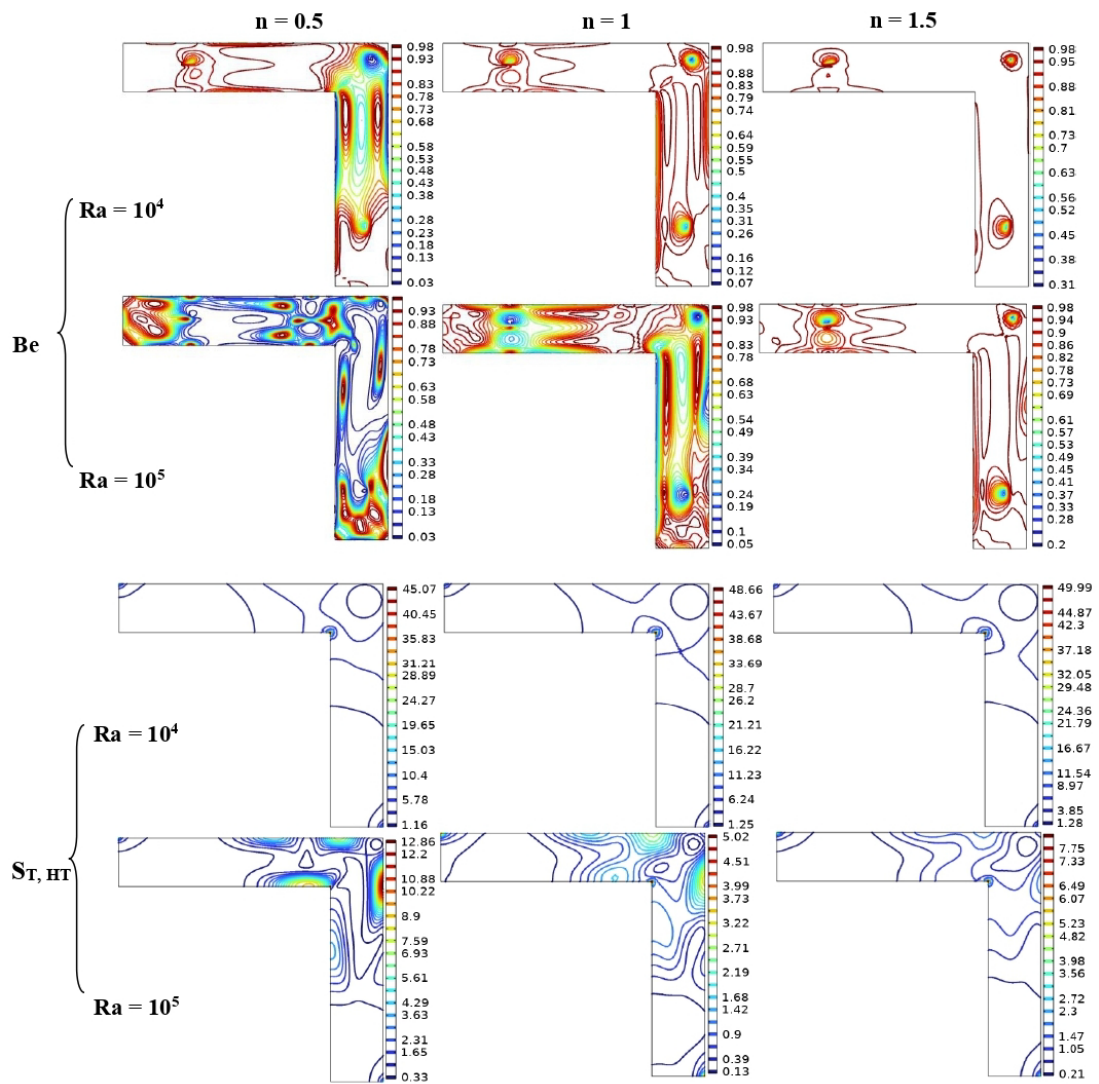
Figure 8. Bejan number (Be) and total entropy due to heat ($S_{T,\,HT}$) for different Ra value and index number (n) at WR = 0.2.
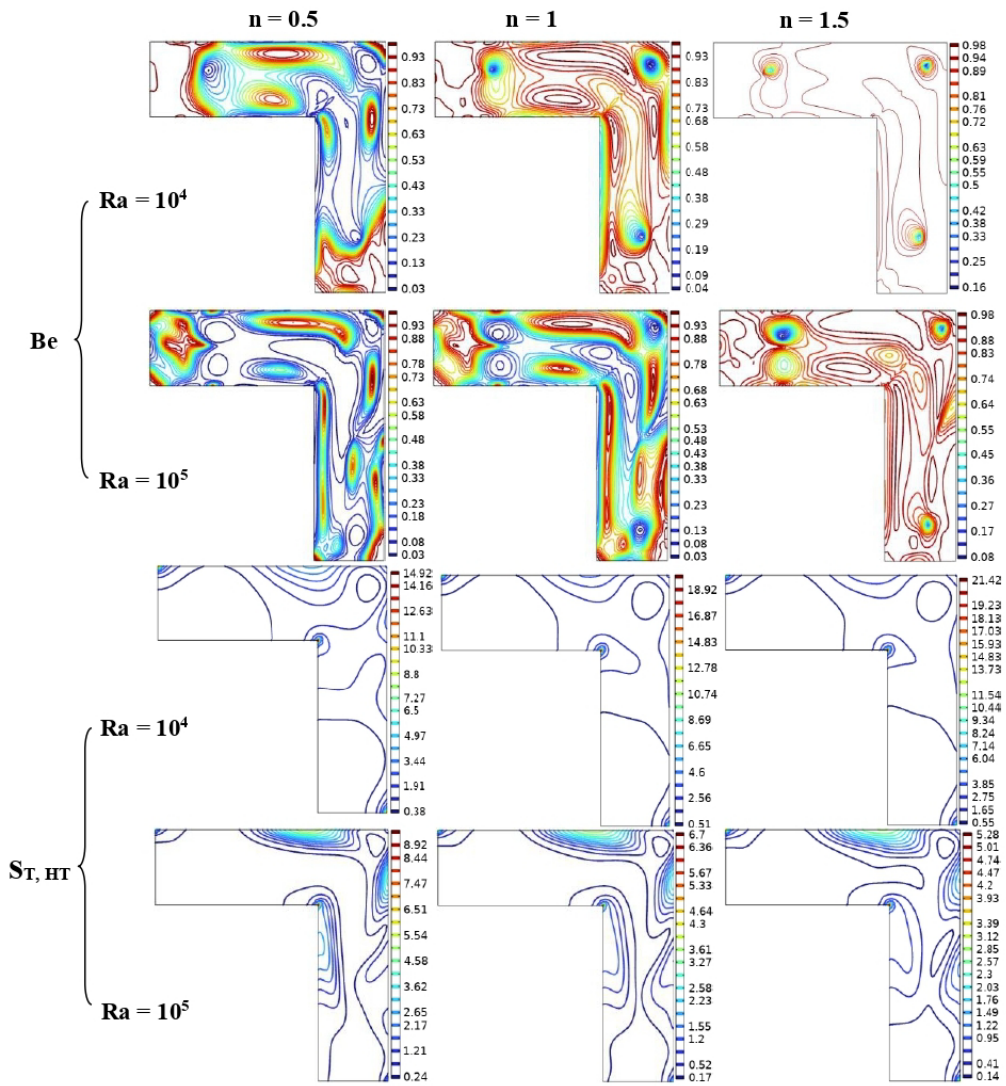
Figure 9. Bejan number (Be) and total entropy due to heat ($S_{T, HT}$) for different Ra values and index number (n) at WR = 0.3.
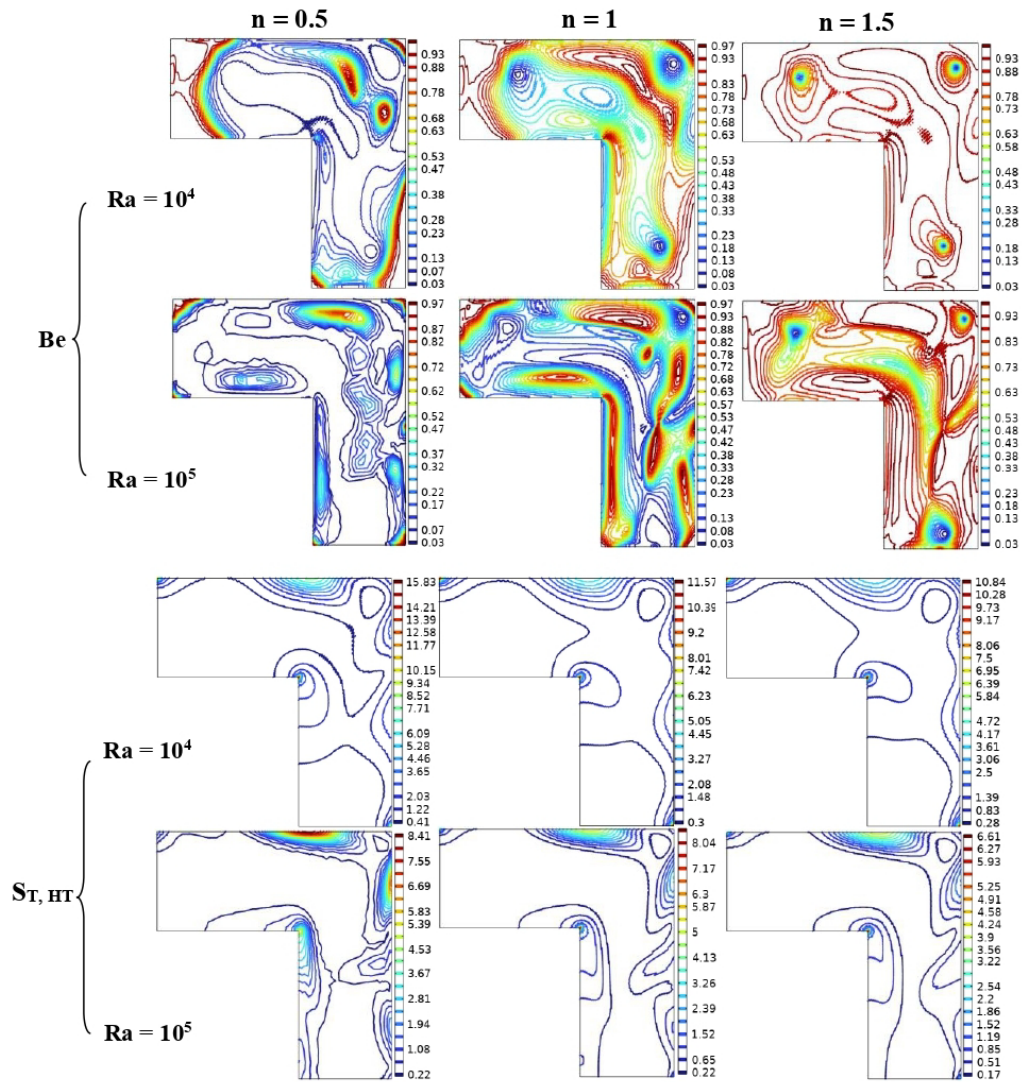
Figure 10. Bejan number (Be) and total entropy due to heat (S$_{T, HT}$) for different Ra values and index number (n) at WR = 0.4.

Figure 11 illustrates the distribution of the local Nu along the vertical and horizontal sides of the heated cavity wall for various n indices and WRs. The local Nu exhibits a more symmetrical shape as the n index decreases and eventually decreases along the hot wall. Moreover, as the n index increases, the shape of the local Nu along the vertical hot wall becomes more asymmetrical, following the same trend as observed for WR = 0.2. With increasing WR, the shape of the local Nu becomes even more asymmetrical. However, as the Ra increases, the maximum magnitude of the local Nu also increases, as demonstrated in Figure 12. This indicates that HT becomes more efficient as Ra increases.

g
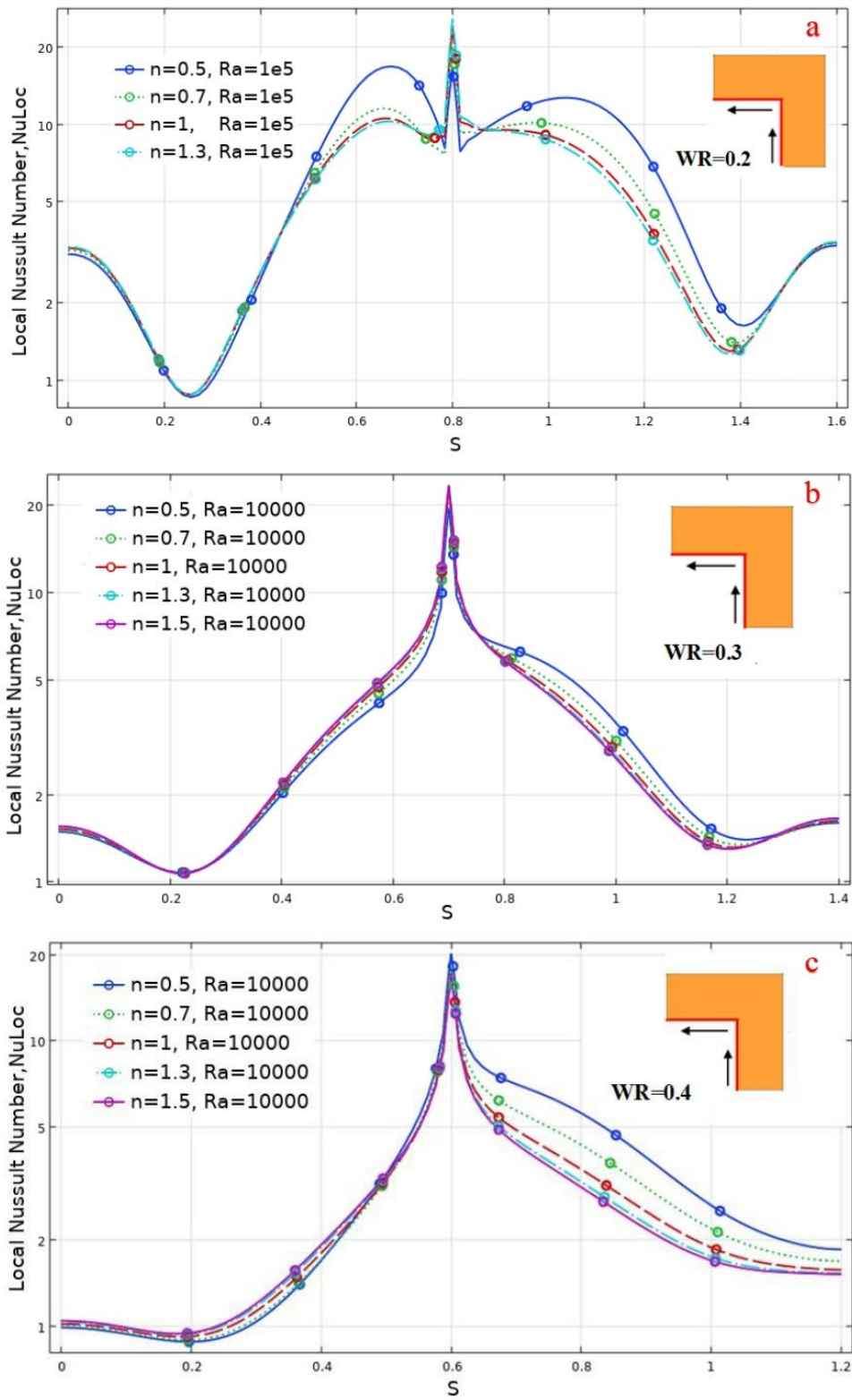
Figure 11. Local Nu along bottom hot walls for different index number (n) and width ratio (WR) at Ra = 10^4.
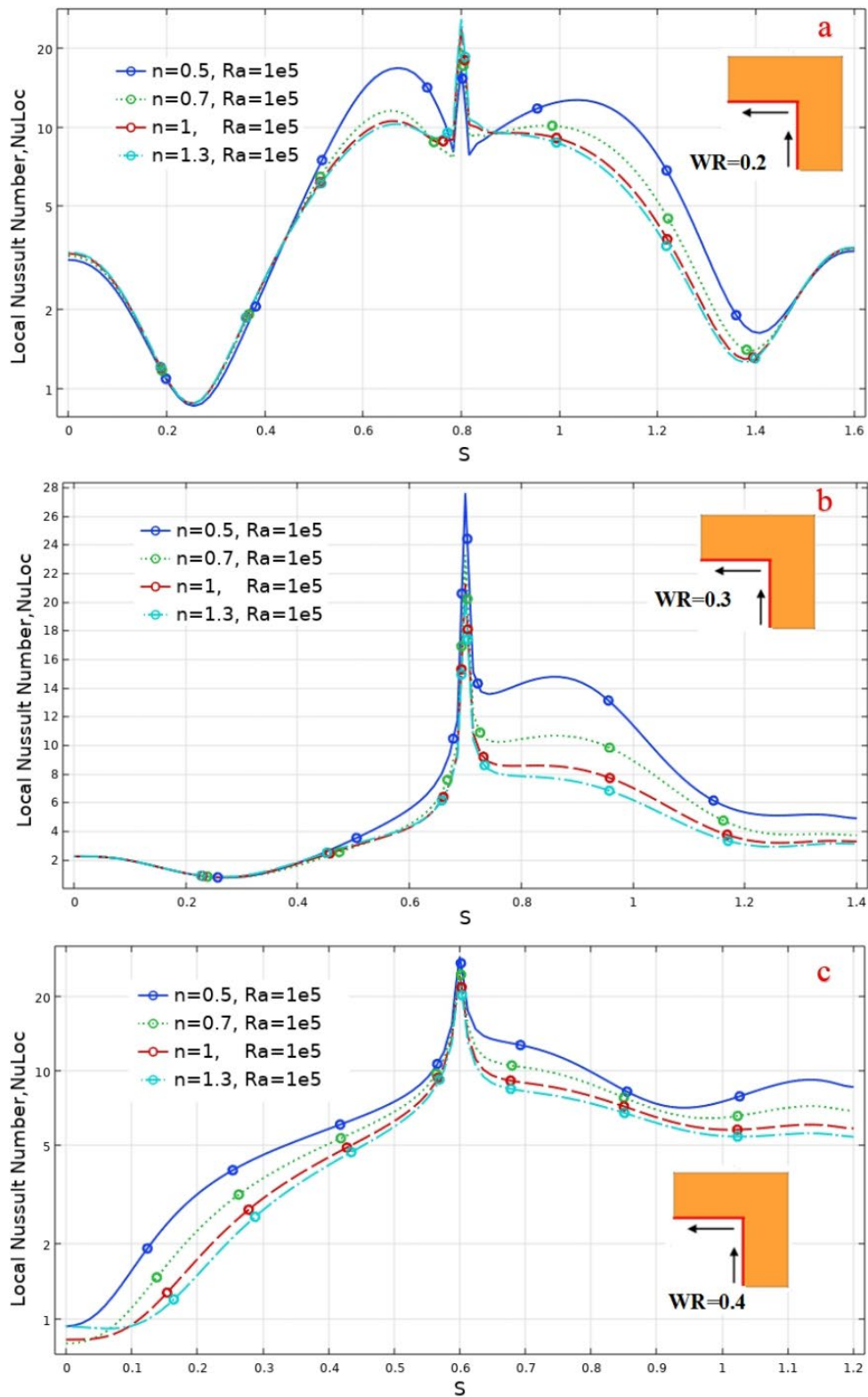
Figure 12. Local Nu along bottom hot walls for different index number (n) and width ratio (WR) at Ra = 10^5.

Figure 13 illustrates the relationship between the average Nu and the Be with respect to the n index for different WR (WR = 0.2, 0.3, and 0.4) and Ra (Ra = 10^4 and 10^5). In Figure 13(a), the behavior of the average Nu in relation to various n indices and WRs is depicted for the range of Ra from 10^4 to 10^5. As the Ra increases, the influence of the n index on the average Nu becomes more pronounced. Specifically, for Ra = 10^5, there is a significant decrease in the average Nu as the n index increases. This decrease is attributed to the dominant role of viscous friction in reducing the HT rate. The maximum average Nu values are achieved at a high WR of 0.4 and a high Ra of 10^5. This is because the buoyancy force at Ra = 10^5 allows for more efficient fluid circulation within the cavity. Increasing the WR from 0.2 to 0.4 enhances the average Nu due to increased fluid circulation at a high Ra of 10^5. However, at a low Ra of 10^4, the average Nu remains relatively constant for WRs of 0.2 and 0.3 as the n index increases, with a slight decrease observed at a high WR of 0.4. Figure 13(b) demonstrates that the Be generally increases as the n index increases for all cases. Since Be corresponds to the irreversibility of heat transfer, a lower Be is desired to enhance the HT rate [43]. At a high Ra of 10^5 and a high WR of 0.4, frictional forces generate more entropy generation, leading to a noticeable decrease in Be.

(a)   (b)
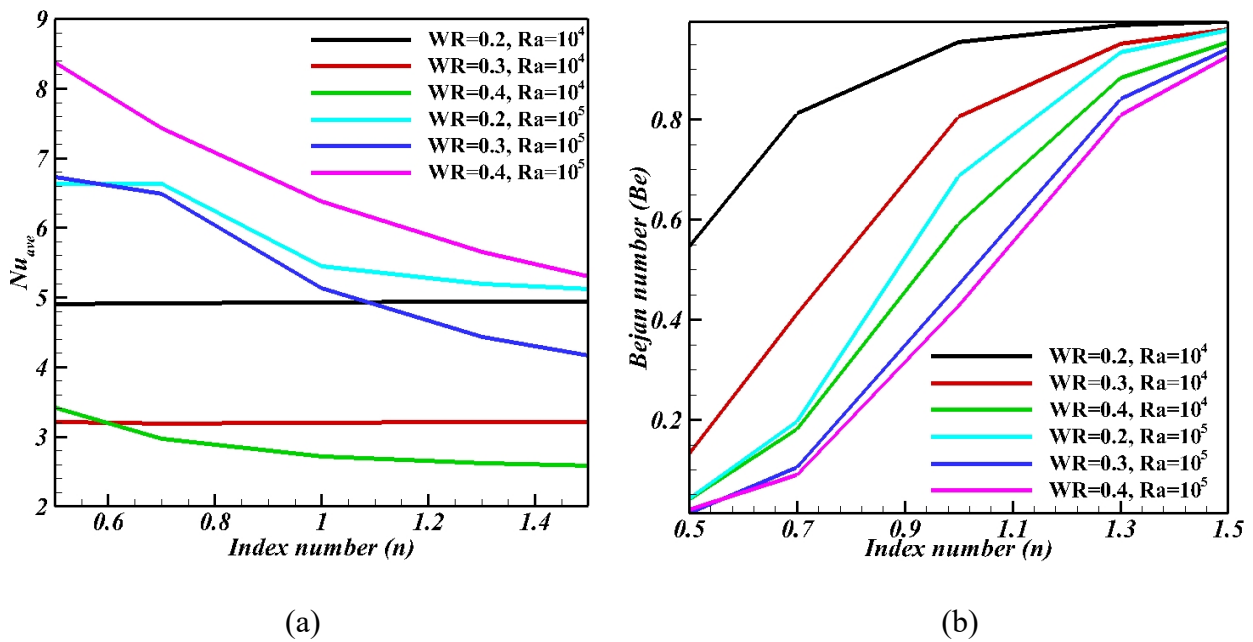
Figure 13. Performance profiles at different Width ratio (WR) and Rayleigh number (Ra): (a) average Nu (Nu$_{ave}$) versus index number (n), and (b) Bejan number (Be) versus index number (n).

Figure 14 presents the total entropy due to heat transfer ($S_{T,\,HT}$) and the total entropy (S_T) as functions of the n index for different width ratios (WR = 0.2, 0.3, and 0.4) and Ra values (Ra = 10^4 and 10^5). Figure 14(a) displays the behavior of $S_{T,\,HT}$ with respect to various n indices and WRs within the range of Ra from 10^4 to 10^5. The minimum $S_{T,\,HT}$ values are achieved at a high Ra of 10^5 and a WR of 0.3, while the maximum $S_{T,\,HT}$ values are observed at a low Ra of 10^4 and a low WR of 0.2. This suggests that the amount of entropy produced due to HT and fluid friction varies with Ra and WR. Figure 14(b) shows that the S_T generally decreases as the n index increases for all cases. This decrease occurs because the convective process slows down as the n index rises, resulting in less fluid movement within the cavity. Consequently, the entropy generated by HT and fluid friction is reduced. Notably, at a high Ra of 10^5 and a high WR of 0.4, frictional forces generate more entropy generation, leading to a significant increase in the S_T.

(a)   (b)
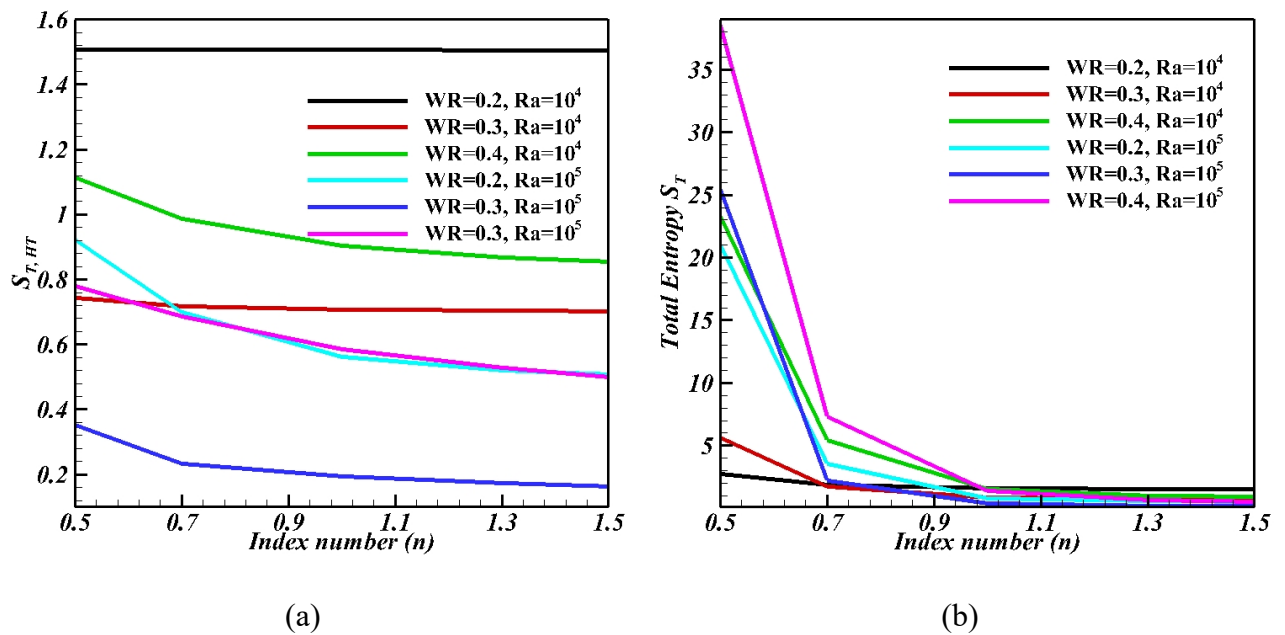
Figure 14. Performance profiles at different Width ratio (WR) and Rayleigh number (Ra): (a) total entropy due to heat transfer ($S_{T,HT}$) versus index number (n), and (b) total entropy (S_T) versus index number (n).

5. Conclusion

In this study, the Finite Difference Lattice Boltzmann Method (FDLBM) was used to examine the natural convection heat transfer (NCHT) and entropy generation (EG) of a non-Newtonian (NN) flow inside an odd-shaped cavity filled with molten polymer. The main examination parameters are Rayleigh number (Ra), Nusselt number (Nu), width ratio (WR), power-law index (n), Prandtl number (Pr), Bejan number

(Be), and total entropy (S_T) due to heat transfer ($S_{T, HT}$). The following highlights were extracted from the study:

- As the Ra increased, heat transfer was enhanced. Unlike dilatant fluids, heat transfer in pseudo-plastic fluids increased as the n index decreased from n = 1 to 0.5.
- The total entropy increased with increasing WR from 0.2 to 0.4 for both Ra = 10^4 and 10^5, while it decreased with an increase in the n index.
- Generally, the average Nu decreased as the n index increased.
- The Be for all WRs exhibited significant increases with the n index. For instance, at WR = 0.2 and Ra = 10^4, the Be values were 0.56 and 0.99 for n = 0.5 and 1.5, respectively.
- The n index had minimal impact on the average Nu at WRs = 0.2 and 0.3, due to low buoyancy force at Ra = 10^4.
- The present model exhibited excellent agreement with previous numerical results, confirming the FDLBM as a superior, reliable, and appropriate technique for relevant applications. This may open the horizon to apply the FDLBM approach in various cavity shapes to interpret the NCHT and EG at different conditions.

References

[1]   A. Henry, Thermal transport in polymers, Annu. Rev. Heat Transf. 17 (2014) 485–520.

[2]   Y. Guo, K. Ruan, X. Shi, X. Yang, J. Gu, Factors affecting thermal conductivities of the polymers and polymer composites: A review, Compos. Sci. Technol. 193 (2020) 108134.

[3]   A. Subba Rao, C.H. Amanulla, N. Nagendra, O. Anwar Beg, A. Kadir, Hydromagnetic flow and heat transfer in a Williamson Non-Newtonian fluid from a Horizontal circular cylinder with Newtonian Heating, Int. J. Appl. Comput. Math. 3 (2017) 3389–3409.

[4]   A. Jahanbakhshi, A.A. Nadooshan, M. Bayareh, Magnetic field effects on natural convection flow of a non-Newtonian fluid in an L-shaped enclosure, J. Therm. Anal. Calorim. 133 (2018) 1407–1416.

[5]   Y. Tizakast, M. Kaddiri, M. Lamsaadi, T. Makayssi, Machine Learning based algorithms for modeling natural convection fluid flow and heat and mass transfer in rectangular cavities filled with non-Newtonian fluids, Eng. Appl. Artif. Intell. 119 (2023) 105750.

[6]   M.Z. Ashraf, S.U. Rehman, S. Farid, A.K. Hussein, B. Ali, N.A. Shah, W. Weera, Insight into significance of bioconvection on MHD tangent hyperbolic nanofluid flow of irregular thickness across a slender elastic surface, Mathematics. 10 (2022) 2592.

[7]   G. Bin Kim, J.M. Hyun, H.S. Kwak, Transient buoyant convection of a power-law non-Newtonian fluid in an enclosure, Int. J. Heat Mass Transf. 46 (2003) 3605–3617.

[8]   M. Ohta, M. Ohta, M. Akiyoshi, E. Obata, A numerical study on natural convective heat transfer of pseudoplastic fluids in a square cavity, Numer. Heat Transf. Part A Appl. 41 (2002) 357–372.

[9]   M. Lamsaadi, M. Naimi, M. Hasnaoui, M. Mamou, Natural convection in a tilted rectangular slot containing Non-Newtonian Power-Law fluids and subject to a longitudinal thermal gradient, Numer. Heat Transf. Part A Appl. 50 (2006) 561–583.

[10]   M. Lamsaadi, M. Naïmi, A. Bahlaoui, A. Raji, M. Hasnaoui, M. Mamou, Parallel flow convection in a shallow horizontal cavity filled with non-Newtonian power-law fluids and subject to horizontal and vertical uniform heat fluxes, Numer. Heat Transf. Part A Appl. 53 (2007) 178–203.

[11]   O. Turan, J. Lai, R.J. Poole, N. Chakraborty, Laminar natural convection of power-law fluids in a square enclosure submitted from below to a uniform heat flux density, J. Nonnewton. Fluid Mech. 199 (2013) 80–95.

[12]   M.H. Matin, I. Pop, S. Khanchezar, Natural convection of power-law fluid between

two-square eccentric duct annuli, J. Nonnewton. Fluid Mech. 197 (2013) 11–23.

[13] L. Khezzar, D. Siginer, I. Vinogradov, Natural convection of power law fluids in inclined cavities, Int. J. Therm. Sci. 53 (2012) 8–17.

[14] M.H. Matin, W.A. Khan, Laminar natural convection of non-Newtonian power-law fluids between concentric circular cylinders, Int. Commun. Heat Mass Transf. 43 (2013) 112–121.

[15] H. Sajjadi, M. Gorji, G.H.R. Kefayati, D.D. Ganji, Lattice Boltzmann simulation of turbulent natural convection in tall enclosures using Cu/water nanofluid, Numer. Heat Transf. Part A Appl. 62 (2012) 512–530.

[16] Y. Shi, G.H. Tang, Non-Newtonian rheology property for two-phase flow on fingering phenomenon in porous media using the lattice Boltzmann method, J. Nonnewton. Fluid Mech. 229 (2016) 86–95. https://doi.org/https://doi.org/10.1016/j.jnnfm.2015.12.002.

[17] J. Su, J. Ouyang, X. Wang, B. Yang, W. Zhou, Lattice Boltzmann method for the simulation of viscoelastic fluid flows over a large range of Weissenberg numbers, J. Nonnewton. Fluid Mech. 194 (2013) 42–59. https://doi.org/https://doi.org/10.1016/j.jnnfm.2012.11.006.

[18] S. Adam, K.N. Premnath, Numerical investigation of the cascaded central moment lattice Boltzmann method for non-Newtonian fluid flows, J. Nonnewton. Fluid Mech. 274 (2019) 104188. https://doi.org/https://doi.org/10.1016/j.jnnfm.2019.104188.

[19] C.R. Leonardi, D.R.J. Owen, Y.T. Feng, Numerical rheometry of bulk materials using a power law fluid and the lattice Boltzmann method, J. Nonnewton. Fluid Mech. 166 (2011) 628–638. https://doi.org/https://doi.org/10.1016/j.jnnfm.2011.02.011.

[20] S.S. Mendu, P.K. Das, Flow of power-law fluids in a cavity driven by the motion of two facing lids – A simulation by lattice Boltzmann method, J. Nonnewton. Fluid Mech. 175–176 (2012) 10–24. https://doi.org/https://doi.org/10.1016/j.jnnfm.2012.03.007.

[21] G.H.R. Kefayati, Simulation of ferrofluid heat dissipation effect on natural convection at an inclined cavity filled with kerosene/cobalt utilizing the Lattice Boltzmann method, Numer. Heat Transf. Part A Appl. 65 (2014) 509–530.

[22] H.R. Ashorynejad, K. Sedighi, M. Farhadi, E. Fattahi, Simulating magnetohydrodynamic natural convection flow in a horizontal cylindrical annulus using the lattice Boltzmann method, Heat Transf. Res. 41 (2012) 468–483.

[23] H.T. Kadhim, A. Al-Manea, A.N. Al-Shamani, T. Yusaf, Numerical analysis of hybrid

nanofluid natural convection in a wavy walled porous enclosure: Local thermal non-equilibrium model, Int. J. Thermofluids. 15 (2022) 100190. https://doi.org/https://doi.org/10.1016/j.ijft.2022.100190.

[24]   A.K. Okab, H.M. Hasan, M. Hamzah, K. Egab, A. Al-Manea, T. Yusaf, Analysis of heat transfer and fluid flow in a microchannel heat sink with sidewall dimples and fillet profile, Int. J. Thermofluids. 15 (2022) 100192. https://doi.org/https://doi.org/10.1016/j.ijft.2022.100192.

[25]   G.H.R. Kefayati, FDLBM simulation of magnetic field effect on non-Newtonian blood flow in a cavity driven by the motion of two facing lids, Powder Technol. 253 (2014) 325–337.

[26]   G.H.R. Kefayati, Simulation of magnetic field effect on non-Newtonian blood flow between two-square concentric duct annuli using FDLBM, J. Taiwan Inst. Chem. Eng. 45 (2014) 1184–1196.

[27]   G.H.R. Kefayati, FDLBM simulation of magnetic field effect on natural convection of non-Newtonian power-law fluids in a linearly heated cavity, Powder Technol. 256 (2014) 87–99.

[28]   M.Y. Jabbar, S.Y. Ahmed, H. Hamazh, F.H. Ali, S.O.W. Khafaji, Effect of layer thickness on natural convection in a square enclosure superposed by nano-porous and non-newtonian fluid layers divided by a wavy permeable wall, Int. J. Mech. Mechatron. Eng. 19 (2019).

[29]   E.D. Aboud, H.K. Rashid, H.M. Jassim, S.Y. Ahmed, S.O.W. Khafaji, H.K. Hamzah, F.H. Ali, MHD effect on mixed convection of annulus circular enclosure filled with Non-Newtonian nanofluid, Heliyon. 6 (2020) e03773.

[30]   M.F. Almensoury, A.S. Hashim, H.K. Hamzah, F.H. Ali, Numerical investigation of natural convection of a non-Newtonian nanofluid in an F-shaped porous cavity, Heat Transf. 50 (2021) 2403–2426.

[31]   F.H. Ali, H.K. Hamzah, K. Egab, M. Arıcı, A. Shahsavar, Non-Newtonian nanofluid natural convection in a U-shaped cavity under magnetic field, Int. J. Mech. Sci. 186 (2020) 105887.

[32]   H.M. Jassim, H.K. Rashid, E.D. Aboud, A.Y. Saba, H.K. Hamzah, F.H. Ali, MHD Mixed Convection in Square Enclosure Filled with non-Newtonian Nanofluid with Semicircular-Corrugated Bottom Wall, Int. J. Mech. Mechatronics Eng. IJMME-IJENS. 20 (2020) 98–114.

[33]   A.K. Hussein, H.K. Hamzah, F.H. Ali, M. Afrand, Natural convection in F-shaped

cavity filled with Ag-water non-Newtonian nanofluid saturated with a porous medium and subjected to a horizontal periodic magnetic field, Korean J. Chem. Eng. 39 (2022) 887–901.

[34] S. Aghakhani, A.H. Pordanjani, A. Karimipour, A. Abdollahi, M. Afrand, Numerical investigation of heat transfer in a power-law non-Newtonian fluid in a C-Shaped cavity with magnetic field effect using finite difference lattice Boltzmann method, Comput. Fluids. 176 (2018) 51–67.

[35] Q.R. Al-Amir, S.Y. Ahmed, H.K. Hamzah, F.H. Ali, Effects of Prandtl number on natural convection in a cavity filled with silver/water nanofluid-saturated porous medium and non-Newtonian fluid layers separated by sinusoidal vertical interface, Arab. J. Sci. Eng. 44 (2019) 10339–10354.

[36] M. Ghalambaz, S.M.H. Zadeh, A. Veismoradi, M.A. Sheremet, I. Pop, Free convection heat transfer and entropy generation in an odd-shaped cavity filled with a Cu-Al2O3 hybrid nanofluid, Symmetry (Basel). 13 (2021) 1–17. https://doi.org/10.3390/sym13010122.

[37] S. Parvin, A.J. Chamkha, An analysis on free convection flow, heat transfer and entropy generation in an odd-shaped cavity filled with nanofluid, Int. Commun. Heat Mass Transf. 54 (2014) 8–17.

[38] F. Ali, H. Jassim, Q. Al-Amir, H. Hamzah, S. Khafaji, Entropy generation analysis of a natural convection inside a sinusoidal enclosure with different shapes of cylinders, Front. Heat Mass Transf. 12 (2018).

[39] G.H.R. Kefayati, Simulation of double diffusive MHD (magnetohydrodynamic) natural convection and entropy generation in an open cavity filled with power-law fluids in the presence of Soret and Dufour effects (part II: entropy generation), Energy. 107 (2016) 917–959.

[40] Z. Cheng, A. Wachs, An immersed boundary/multi-relaxation time lattice Boltzmann method on adaptive octree grids for the particle-resolved simulation of particle-laden flows, J. Comput. Phys. 471 (2022) 111669.

[41] G. Kefayati, An immersed boundary-lattice Boltzmann method for thermal and thermo-solutal problems of Newtonian and non-Newtonian fluids, Phys. Fluids. 32 (2020) 073103.

[42] R.R. Huilgol, G.H.R. Kefayati, From mesoscopic models to continuum mechanics: Newtonian and non-Newtonian fluids, J. Nonnewton. Fluid Mech. 233 (2016) 146–154.

[43] Q.R. Al-Amir, H.K. Hamzah, F.H. Ali, M. Hatami, W. Al-Kouz, A. Al-Manea, R. Al-Rbaihat, A. Alahmer, Investigation of Natural Convection and Entropy Generation in a Porous Titled Z-Staggered Cavity Saturated by TiO2-Water Nanouid, Int. J. Thermofluids. 19 (2023) 100395.

Nomenclature

	Nomenclature		
A, B	Polynomial constant parameters	F	Interface locations
AR	Aspect ratio of the cavity	T_o	Average temperature
Be	Bejan number	S_T	Total entropy
c_k	Discrete particle velocity	$S_{T,HT}$	Total entropy due to heat transfer
C_p	Specific heat (KJ/kg.K)	NCHT	Natural convection heat transfer
Da	Darcy number	Mag. Fld.	magnetic field
EG	Entropy generation	HT	Heat transfer
Ha	Hartmann number	NN	Non-Newtonian
f_k^{eq}	Equilibrium distribution function	Nu_{Loc}	Local Nusselt number
g	Gravitational acceleration (m/s^2)	Nu_{ave}	Average Nusselt number
k	Thermal conductivity (W/m.K)	$Ü$	Dimensionless velocity component in x-direction
k	Node number	Ri	Richardson number
K	Consistency	N	Normal vector
L	Length of cold or hot wall (m)	ü	Velocity component in x-direction (m/s)
$\ddot{p}$	Dimensionless pressure	$\ddot{V}$	Dimensionless velocity component in y-direction
$\ddot{p}$	Pressure (Pa)	W	Width (m)
n	Power-law index	$\ddot{v}$	Velocity component in y-direction (m/s)
Gr	Grashof number	S	The distance along the bottom hot walls
Pr	Prandtl number (ν_f/α_f)	$\ddot{X}$	Dimensionless coordinate in the horizontal direction
Ra	Rayleigh number ($g\beta_f L^3 \Delta T / \nu_f \alpha_f$)	$\ddot{x}$	Cartesian coordinates in the horizontal direction (m)
T	Temperature (K)	$\ddot{Y}$	*Dimensionless coordinate in the vertical direction*
T_c	*Temperature of the cold surface (K)*	$\ddot{y}$	Cartesian coordinates in the vertical direction (m)
O	Error term	t	*Time (sec)*
T_h	Temperature of the hot surface (K)		
	Greek symbols		
α	Thermal diffusivity (m^2/s)	ν	Kinematic viscosity (μ /ρ) (Pa. s)
$\bar{\theta}$	Dimensionless temperature (T-Tc/Th-Tc)	Γ	Irreversibility factor
Ψ	Dimensional stream function (m^2/s)	ε	Time step
ψ	Dimensionless stream function	β	Volumetric coefficient of thermal expansion (K^{-1})
μ	Dynamic viscosity (kg.s/m)	ρ	Density (kg/m^3)
ω	Relaxation time	Ω_k	Rate of change of f_k^{eq}
$\ddot{M}_a$	Apparent viscosity	$\tau_{i,j}$	Shear stress tensor
φ	Solid volume fraction	λ	Periodic shape parameter